Quantitative single-cell spatial mapping of bone marrow architecture defines a tissue-state biomarker for disease activity and therapeutic response in myelodysplastic neoplasms

One Sentence Summary: A spatially resolved bone marrow tissue-state biomarker improves assessment of disease activity and remission beyond blast counts in myelodysplastic neoplasms.

Ryan Nachman,[1] Aleksandra Kopacz,[1] Caitlin Unkenholz,[1,4] Jian Chai, [2] Arvin Ruiz,[3] Itzel Valencia,[4] Jeanne Jiang,[4] Fabio Socciarelli,[4] Jiwoon Park,[5] Christopher E. Mason,[(5-8)] Ling Zhang,[9] David Sallman,[10] Gail J. Roboz,[11] Pinkal Desai,[11] Justin Kaner,[11] Joshua Fein,[11] Monica Guzman,[11] Neal Lindeman,[12] Amy Chadburn,[2] Madhu Ouseph,[2,12] Paul Simonson,[2] Julia Geyer,[2] Giorgio Inghirami,[2,3] Shahin Rafii,[1] David Redmond,[1*] Sanjay S. Patel[2,4*]

[1]Division of Regenerative Medicine, Hartman Institute for Therapeutic Organ Regeneration, Ansary Stem Cell Institute, Department of Medicine, Weill Cornell Medicine, New York, NY, USA

[2]Division of Hematopathology, Department of Pathology and Laboratory Medicine, Weill Cornell Medicine/NewYork-Presbyterian Hospital, New York, NY, USA [s]

[3]Immunopathology Laboratory, Weill Cornell Medical College/NewYork-Presbyterian Hospital, New York, NY, USA

[4]Multiparametric In Situ Imaging (MISI) Laboratory, Department of Pathology and Laboratory Medicine, Weill Cornell Medicine, New York, NY, USA

[5]Department of Physiology and Biophysics, Weill Cornell Medicine, New York, NY, USA

[6]The Feil Family Brain and Mind Research Institute, Weill Cornell Medicine, New York, NY

[7]WorldQuant Initiative for Quantitative Prediction, Weill Cornell Medicine, New York, NY

[8]The HRH Prince Alwaleed Bin Talal Bin Abdulaziz Alsaud Institute for Computational Biomedicine, Weill Cornell Medicine, New York, NY

[9]Department of Hematopathology and Laboratory Medicine, Moffitt Cancer Center, Tampa, FL, USA

[10]Department of Malignant Hematology, Moffitt Cancer Center, Tampa, FL, USA

[11]Division of Hematology and Medical Oncology, Department of Medicine, Weill Cornell Medicine/NewYork-Presbyterian Hospital, New York, USA

[12]Division of Molecular Genetic Pathology, Department of Pathology and Laboratory Medicine, Weill Cornell Medicine/NewYork-Presbyterian Hospital, New York

*Correspondence: Sanjay Patel, MD (sap9151@med.cornell.edu) & David Redmond, PhD (dar2042@med.cornell.edu) | Abstract word count: 206 | Main text word count (incl. Methods): ~4,860 | Main Table Count: 0 | Main Figure count: 7 | References: 47 | Supplemental Table count: 6 | Supplemental Figure count: 10

ABSTRACT

Assessment of myelodysplastic neoplasms (MDS) relies on histomorphology and blast enumeration, metrics that incompletely capture marrow architecture and disease state during therapy. We developed a quantitative spatial profiling platform to define a tissue-level biomarker of MDS using whole-slide multiplex immunofluorescence imaging and single-cell phenotyping. Diagnostic biopsies (n=36), longitudinal treatment samples (n=29), precursor states (n=13), and normal controls (n=21) were analyzed, comprising >5 million spatially resolved cells. MDS marrow exhibited coordinated, genotype-imprinted microarchitectural remodeling, including altered progenitor composition and spatial patterning, disrupted erythroid topology, and displacement of hematopoietic stem and progenitor cells from perivascular niches. We evaluated 82 cellular and spatial features and designed a weighted composite metric, the MDS Microarchitectural Perturbation Score (MDS-MAPS), derived from diagnostic samples and locked before longitudinal analysis. In leave-one-patient-out cross-validation, MDS-MAPS discriminated remission from active disease more accurately than blast percentage (AUC 0.883 vs 0.660; average precision 0.567 vs 0.250) and outperformed mutation burden–based metrics in distinguishing low-blast MDS from CCUS (AUC 0.815; average precision 0.890). Mixed-effects modeling showed MAPS decreased in remission independent of blast burden, with architectural normalization at remission and re-emergence of spatial perturbations at relapse. These findings define quantitative marrow architecture as a dynamic, clinically deployable tissue-state biomarker that complements molecular and blast-based assessment in MDS.

INTRODUCTION

Myelodysplastic neoplasms (MDS) arise from clonal hematopoietic stem and progenitor cells and are characterized by ineffective hematopoiesis, peripheral cytopenias, and risk of progression to acute myeloid leukemia (1). Diagnosis and disease assessment rely heavily on histopathologic evaluation of bone marrow biopsies, including subjective assessment of dysplasia and manual enumeration of blast percentage (2, 3). Although these approaches remain central to clinical decision-making, they provide limited quantitative insight into the spatial organization of the marrow and may incompletely capture the biological state of the disease.

Genomic profiling has substantially advanced understanding of the cell-intrinsic drivers of MDS and has improved risk stratification models (4). However, most molecular and immunophenotypic data are derived from peripheral blood or aspirated marrow, which lack preservation of tissue architecture and spatial cellular interactions. As a result, while hundreds of thousands of cells can be profiled in suspension, the spatial organization of hematopoiesis within intact marrow—where both cell-intrinsic and microenvironmental influences converge—remains poorly quantified. Reliable models that integrate spatial architecture with the clinical and genetic heterogeneity of MDS are still lacking (5, 6).

We recently established a platform for in situ spatial mapping of human hematopoiesis using multiplex immunofluorescence, whole-slide imaging, and single-cell–resolved image analysis, revealing conserved architectural patterns in normal aging marrow (7). Here, we apply and extend this framework to clinically and genetically annotated MDS biopsies, including longitudinal samples obtained during therapy. We hypothesized that quantitative measures of bone marrow microarchitecture capture a tissue-level disease state that complements conventional metrics. By integrating spatial features into a composite MDS Microarchitectural Perturbation Score (MDS-MAPS), we test whether marrow architecture encodes clinically relevant information across diagnostic and serial samples and whether it dynamically reflects disease remodeling over time.

RESULTS

73 ***Characteristics of patient cohort***

74 We assembled a cohort of clinically and genetically annotated archival bone marrow trephine biopsy
75 samples collected as part of routine diagnostics at our academic medical center **(Figure 1a, Supplementary Data**
76 **Table 1)**. The cohort included 77 samples from 49 unique patients with either MDS (n=36) or the precursor state
77 clonal cytopenia of unknown significance (CCUS, n=13); additionally, for 14 of the MDS patients, 29 serial
78 samples collected along the course of pharmacologic management, with or without eventual allogeneic
79 hematopoietic stem cell transplantation (HSCT), were also profiled. 21 normal bone marrow controls (NBMs),
80 including age-matched samples, from a recently published cohort were also analyzed (7). All cross-sectional
81 analyses were performed on diagnostic samples unless otherwise stated (Figures 1-6 data). Remission
82 classification analyses included only MDS samples with annotated clinical status (Figure 7 data).

83 The median age among CCUS and MDS patients was 77, with a M:F of 1:1. MDS samples were
84 categorized into those with low-blasts (MDS-LB, n=20) or with high-blasts (MDS-IB, n=16). International
85 Prognostic Scoring System-Molecular (IPSS-M) values were calculated for all diagnostic samples from MDS
86 patients. IPSS-M scores ranged from –1.61 to 4.39 (median=0.285); cases were subclassified by risk class into
87 Very Low (n=1), Low (n=6), Moderate Low (n=7), Moderate High (n=3), High (n=5), and Very High (n=10).

88 ***Quantitative and morphologic variations between normal and MDS bone marrows***

89 Following multiplex immunofluorescence (MxIF) staining and whole-slide imaging (WSI) of trephine
90 biopsy tissues, individual cells and structural landmarks were segmented and phenotyped at single-cell resolution
91 as previously described, yielding a dataset of 5,146,986 spatially resolved cells (**Figure 1b-f, Supplementary**
92 **Data Figure 1a-b**) (7).

93 Quantitative cell-type proportions derived from MxIF—including myeloblasts, promyelocytes, erythroid
94 normoblasts, and maturing myeloid cells (MMCs)—correlated with orthogonal measurements from manual

differential counts and multiparameter flow cytometry (**Supplementary Data Figure 1c**, **Supplementary Data Table 2**), supporting the analytical validity of the approach.

Comparative analysis across NBMs and treatment-naïve CCUS, MDS-LB, and MDS-IB samples revealed progressive remodeling of hematopoietic composition and morphology with disease severity (**Figure 2**). HSPCs, myeloblasts, and megakaryocytes increased commensurate with higher-risk disease (**Figure 2a**, **Supplementary Data Figure 2a**), consistent with prior aspirate-based studies (8) but now contextualized within intact marrow architecture. Megakaryocyte expansion in MDS-IB was accompanied by enrichment of smaller, frequently mononuclear forms; quantitative assessment of nuclear number and cell area confirmed this shift (**Figure 2b–c**). CD34-expressing megakaryocytes were present in all groups but were most frequent in *TP53*-mutated MDS-IB samples (**Supplementary Data Figure 2d**). Erythroid normoblasts demonstrated increased cell area in MDS relative to age-matched NBMs and CCUS (**Supplementary Data Figure 2e**), whereas early erythroid and myeloid precursors exhibited genotype-dependent size variation, with the smallest proerythroblasts and promyelocytes observed in *TP53*-mutated cases (**Supplementary Data Figure 2f**).

Genotype-specific compositional signatures were evident. *TP53*-mutated MDS samples displayed marked depletion of promyelocytes and MMCs, alongside expansion of proerythroblasts and maturing erythroid normoblasts relative to other MDS-IB samples (**Figure 2d**). p53 protein labeling has been well-described as a method for identifying mutant p53 protein-containing cells (putative *TP53*-mutated cells) in tissue sections (9–11). Integration of p53 protein labeling with MxIF enabled in situ identification of putative *TP53*-mutated cells, which were enriched within myeloblast and erythroid precursor compartments (**Figure 2e–g**, **Supplementary Data Figure 2c**). In contrast, endothelial cell proportions did not differ significantly across disease states (**Supplementary Data Figure 2b**).

Collectively, these findings demonstrate reproducible, genotype-imprinted alterations in marrow cellular composition and morphology that extend beyond conventional blast enumeration and risk classification.

118 ***HSPCs and early hematopoietic progenitors are progressively displaced from perivascular and para-trabecular***
119 ***zones along progression from clonal hematopoiesis to overt MDS***

120 In normal bone marrow, hematopoietic stem and progenitor cells (HSPCs) localize preferentially to
121 perivascular and para-trabecular niches (7). Consistent with our prior findings, HSPCs in young and older NBMs
122 were significantly enriched within 15µm of CD34+ endothelial-lined vasculature (**Figure 3a–c**, **Supplementary**
123 **Data Figure 3a–b**). This enrichment pattern was largely preserved in CCUS samples. In contrast, HSPCs in both
124 MDS-LB and MDS-IB samples were significantly displaced from vasculature, exhibiting increased average
125 distances relative to NBMs and precursor states (**Figure 3c–d**, **Supplementary Data Figure 3a–b**). Within MDS
126 samples, HSPCs were positioned farther from vasculature than most other hematopoietic cell types
127 (**Supplementary Data Figure 3b**), indicating a selective disruption of the normal perivascular niche.

128 A similar exclusionary pattern was observed for myeloblasts, while promyelocytes demonstrated
129 significant displacement primarily in MDS-IB (**Figure 3c**, **Supplementary Data Figure 3a**). In contrast, CD38+
130 small hematolymphoid cells and megakaryocytes remained consistently enriched near vasculature across disease
131 states, with megakaryocytes showing relative enrichment in MDS samples (**Figure 3c**, **Supplementary Data**
132 **Figure 3a–b**). These findings indicate remodeling of perivascular cellular composition in MDS.

133 To determine whether clonal genotype influenced spatial localization, we leveraged p53 protein labeling
134 to distinguish putative *TP53*-mutated from wild-type (WT) HSPCs. WT-HSPCs remained relatively proximal to
135 endothelium, whereas *TP53*-mutated HSPCs were significantly displaced (**Figure 3e–f**, **Supplementary Data**
136 **Figure 3e**). This genotype-specific pattern suggests that clonal HSPCs contribute disproportionately to
137 perivascular niche disruption in *TP53*-mutated disease.

138 Given the established role of CXCL12–CXCR4 signaling in HSPC homing to the vascular niche,(12) we
139 examined publicly available transcriptomic and proteomic datasets of MDS samples (13–16). Re-analysis
140 revealed consistently reduced CXCR4 expression within HSPC populations from MDS patients relative to healthy

141 controls (**Supplementary Data Figure 4**). Across four independent RNA sequencing datasets, *CXCR4* was the
142 only gene significantly and reproducibly downregulated in HSPC compartments (**Supplementary Data Figure**
143 **4d**). These findings provide a potential molecular correlate for impaired perivascular localization in MDS.

144 In contrast to vascular displacement, HSPC enrichment near bone trabeculae was largely preserved across
145 disease states, although average distances increased modestly in MDS-LB and MDS-IB samples (**Supplementary**
146 **Data Figure 3c–d**). Promyelocytes and myeloblasts, however, exhibited more widespread disruption of normal
147 para-trabecular localization in MDS (**Supplementary Data Figure 3c–d**).

148 Collectively, these analyses demonstrate selective displacement of early hematopoietic progenitors from
149 perivascular niches in MDS, with pronounced effects in *TP53*-mutated disease and accompanying alterations in
150 *CXCR4* expression, highlighting spatial remodeling of key regulatory microenvironments.

151 ***Atypical erythroid island formation in MDS***

152 Erythroid normoblasts in normal bone marrow are organized into well-formed maturation "islands," a
153 structural feature readily appreciated by light microscopy. Disaggregation of these islands has been described in
154 advanced MDS (17–20), but systematic, quantitative assessment of erythroid spatial organization and its
155 relationship to genotype and clinical parameters has not been previously performed.

156 Whole-slide erythroid phenotype mapping revealed large, cohesive erythroid aggregates in NBMs, with
157 progressive disaggregation in MDS samples, particularly in MDS-IB (**Figure 4a–b**, **Supplementary Figure 5a**).
158 At the single-cell level, erythroid normoblasts in MDS were separated by significantly greater nearest-neighbor
159 distances compared with NBMs and CCUS samples (**Figure 4c**), indicating reduced clustering.

160 To quantify erythroid spatial organization across treatment-naïve samples, we applied a Rolling Signal–
161 based Ripley's K analysis to measure aggregation across increasing spatial radii (**Figure 4d**). NBMs exhibited
162 the highest K-ratios, reflecting robust clustering, whereas the lowest K-ratios were observed in *TP53*-mutated

163 MDS-IB samples (**Figure 4e**). Notably, *SF3B1*-mutated MDS-LB samples also demonstrated reduced clustering
164 relative to mutation-negative MDS-LB and MDS-IB cases, indicating genotype-specific distortion of erythroid
165 topology independent of blast burden. Erythroid cluster density analyses yielded concordant results
166 (**Supplementary Data Figure 5b–c**).

167 Importantly, the K-ratio correlated positively with peripheral blood hemoglobin levels (**Figure 4f**), linking
168 quantitative disruption of erythroid island architecture with clinical anemia severity. Together, these findings
169 demonstrate that erythroid island disaggregation is a measurable and genotype-imprinted feature of MDS
170 microarchitecture and that quantitative spatial metrics capture clinically relevant aspects of ineffective
171 hematopoiesis not discernible by conventional morphology alone.

172 ***Atypical localization of immature precursors (ALIP) correlates with disease severity and discriminates TP53-***
173 ***mutated and -WT subtypes of high-risk MDS***

174 In normal bone marrow, immature granulocytic precursors localize preferentially near bone trabeculae
175 and vasculature, with progressive maturation occurring toward medullary regions. Atypical localization of
176 immature precursors (ALIP) describes the abnormal clustering of myeloblasts and promyelocytes distant from
177 these regulatory niches and has historically been associated with adverse cytogenetic features and inferior
178 outcomes (21, 22)**.** However, ALIP has largely been assessed qualitatively, without systematic whole-slide
179 quantification.

180 Using multiplex imaging and spatial mapping, we identified discrete foci of ALIP in a subset of MDS
181 samples (**Figure 5a–b**). We operationally defined ALIP as clusters of two or more myeloblasts and/or
182 promyelocytes within 12µm of one another located >150µm from trabeculae and >40µm from vasculature.
183 Whole-slide analyses revealed marked variation in ALIP frequency and distribution across NBMs, CCUS, and
184 MDS samples (**Figure 5c**).

185 Among treatment-naïve MDS cases, ALIP cluster density increased with disease severity, with the highest
186 densities observed in many MDS-IB samples (**Figure 5d–e**, **Supplementary Data Figure 6**). Notably, within
187 the MDS-IB group, *TP53*–wild-type higher-risk cases exhibited greater ALIP cluster density than *TP53*-mutated
188 counterparts (**Figure 5d–e**), revealing spatial heterogeneity within clinically similar high-risk disease categories.
189 These patterns were robust to correction for cellularity and alternative cluster definitions.

190 These findings demonstrate that whole-slide quantification of ALIP uncovers genetically imprinted spatial
191 heterogeneity in MDS that may not be captured by conventional risk stratification frameworks, reinforcing the
192 concept that microarchitectural organization provides complementary information to blast enumeration and
193 clinical scoring systems.

194 ***Integration of single cell quantitative features and microarchitectural patterns to generate a spatially informed***
195 ***Microarchitectural Perturbation Score (MAPS)***

196 To determine whether the diverse cellular and spatial perturbations observed across MDS samples could
197 be integrated into a unified representation of tissue state, we aggregated single-cell morphologic features, cell-
198 type proportions, spatial relationships, and microenvironmental localization metrics into a composite parameter
199 termed the MDS Microarchitectural Perturbation Score (MDS-MAPS) (**Figure 6a**).

200 Dimensionality reduction of sample-level feature matrices demonstrated clear separation between NBMs
201 and treatment-naïve MDS samples (**Figure 6b**, **Supplementary Data Figure 7a**). Within MDS cases, *TP53*-
202 mutated samples formed a distinct cluster independent of blast category, whereas *TP53*–wild-type MDS-LB and
203 MDS-IB samples distributed along a continuum corresponding broadly to IPSS-M–defined risk strata. Feature
204 importance analyses identified contributions from multiple domains—including progenitor displacement,
205 erythroid clustering disruption, megakaryocyte morphometrics, and ALIP density (**Supplementary Data Figure**
206 **7c**).

207 To assess spatial heterogeneity within individual tissues, we computed 82 quantitative features at the
208 256µm patch level and projected patch-level observations into reduced-dimensional space (**Supplementary Data**
209 **Figure 7b**). Patch-level MAPS values were derived using weights informed by disease severity stratification
210 (**Supplementary Data Figure 7c**), enabling visualization of localized perturbations across whole-slide sections
211 (**Figure 6c**).

212 Heatmap overlays revealed marked intra-tissue heterogeneity in many MDS samples. Mean MDS-MAPS
213 values increased with morphologic severity, with the highest scores observed in *TP53*-mutated cases (**Figure 6d–**
214 **e**, **Supplementary Data Figure 7d**). Notably, several patients categorized as lower risk by IPSS-M exhibited
215 elevated MDS-MAPS values (WCM6, WCM27, WCM29, WCM49, WCM50, WCM51, WCM77), and these
216 discordant samples displayed focal features typically associated with higher-risk disease. MDS-LB samples
217 demonstrated the greatest entropy of patch-level MAPS values (**Figure 6e**), indicating substantial spatial
218 heterogeneity at earlier disease stages.

219 In addition, focal regions with elevated MAPS were detected in selected CCUS samples. These localized
220 perturbations exhibited architectural features characteristic of overt MDS, suggesting that quantitative spatial
221 mapping may detect early microarchitectural remodeling not readily apparent by conventional histopathology.
222 These observations remain hypothesis-generating and warrant prospective validation.

223 Collectively, these analyses establish MDS-MAPS as a quantitative tissue-level metric that integrates
224 cellular composition, morphology, and spatial topology to represent the degree and heterogeneity of marrow
225 architectural perturbation across genetic and clinical strata.

226 To determine whether MDS-MAPS could discriminate precursor states from overt low-risk disease, we
227 performed leave-one-patient-out cross-validation comparing treatment-naïve CCUS (n=13) and MDS-LB (n=20)
228 samples. MDS-MAPS demonstrated strong discrimination (AUC=0.815; average precision=0.890),
229 outperforming mutation burden–based metrics including maximum and summed variant allele frequency

230 (**Supplementary Data Figure 8**). These findings indicate that quantitative microarchitectural perturbation
231 distinguishes CCUS from morphologically defined low-blast MDS and captures tissue-level disease features not
232 reflected by clonal burden alone.

233 ***Correlation of cell morphologic and spatial features with blast progression***

234 Because blast percentage remains central to clinical prognostication models such as IPSS-R and IPSS-M
235 (4, 23), we examined whether quantitative spatial and morphologic parameters derived from multiplex imaging
236 were associated with subsequent blast progression in the subset of diagnostic MDS samples from patients who
237 later received disease-modifying therapies (n=16) (**Supplementary Data Table 3**).

238 Using modeling approaches appropriate for limited sample sizes, we evaluated the relationship between
239 extracted spatial features and subsequent blast count increase. Models incorporating multiplex imaging–derived
240 parameters demonstrated improved discrimination of blast progression relative to models based solely on standard
241 clinical risk variables (**Supplementary Data Figure 9a**). While MDS-MAPS broadly tracked with IPSS-M
242 scores, multiple samples exhibited discordant risk estimates between these frameworks (**Supplementary Data**
243 **Figure 9b**), suggesting that spatial architecture captures complementary dimensions of disease biology.

244 Among individual features, displacement of promyelocytes from perivascular niches emerged as one of
245 the most strongly associated spatial parameters with blast progression, demonstrating greater rank-based
246 significance than conventional clinical variables (**Supplementary Data Figure 9c–d**). These findings indicate
247 that microarchitectural remodeling—particularly disruption of early progenitor niche localization—may reflect
248 dynamic disease biology relevant to blast evolution.

249 Given the limited cohort size, these analyses are exploratory and hypothesis-generating. However, they
250 suggest that quantifiable spatial features derived from whole-slide imaging may provide additive prognostic
251 information beyond conventional blast enumeration and established risk scoring systems, warranting prospective
252 validation in larger cohorts.

253 ***Multimodal longitudinal assessment in the course of disease modifying therapies***

254 Longitudinal biopsies were analyzed from 14 MDS patients treated with growth factor therapy and/or
255 hypomethylating agents, with or without venetoclax; three patients additionally underwent allogeneic stem cell
256 transplantation. Among pharmacologically treated patients, three achieved clinical remission (WCM2, WCM13,
257 WCM44), and three additional patients achieved remission following transplantation (WCM17, WCM21,
258 WCM46).

259 Across serial samples, MDS-MAPS values were consistently reduced in remission biopsies relative to
260 active disease (**Figure 7a**). Paired within-patient analyses demonstrated significant decreases in MAPS at
261 remission timepoints, including in cases with molecular remission (**Figure 7b**), indicating that architectural
262 normalization accompanies clinical and genetic response.

263 To evaluate whether MAPS could discriminate remission status in unseen patients, we performed logistic
264 regression with leave-one-patient-out cross-validation (LOPO-CV), thereby avoiding within-patient data leakage.
265 Across serial samples, MAPS demonstrated superior discrimination of remission versus active disease compared
266 with blast percentage, as measured by both area under the receiver operating characteristic curve (AUC) and
267 average precision (AP) in precision–recall analysis (**Figure 7c**). Notably, inclusion of blast percentage did not
268 materially improve model performance, suggesting that MAPS captures dominant and partially orthogonal
269 information regarding disease state.

270 Mixed-effects modeling accounting for patient-level variability revealed that MAPS decreased
271 significantly in remission independent of blast burden (**Figure 7d**), supporting the interpretation that MAPS
272 reflects large-scale architectural remodeling rather than merely tracking blast percentage. While MAPS correlated
273 with established clinical risk metrics, discordance in several samples underscores that it quantifies distinct aspects
274 of marrow organization (**Figure 7e**).

275 Representative longitudinal trajectories from patients WCM13 and WCM44 illustrate dynamic
276 remodeling of marrow architecture across treatment courses (**Supplementary Figure 10a)**. Remission samples

277 embedded closer to NBMs in reduced-dimensional feature space and returned toward an MDS-associated profile
278 at relapse (**Supplementary Figure 10b**). In patient WCM44, transient re-localization of HSPCs to perivascular
279 niches was observed at remission (**Supplementary Figure 10c**); remission in both patients was accompanied by
280 normalization of ALIP density, erythroid clustering, and megakaryocyte morphometrics (**Supplementary Figure**
281 **10d**).
282
283 Although limited by sample size, these findings provide proof-of-principle that quantitative spatial
284 architecture represents a dynamic and clinically informative tissue-state variable that tracks therapeutic response
285 and complements conventional blast-based assessment.
286
287 **DISCUSSION**
288 The spatial microarchitecture of hematopoiesis in the bone marrow remains incompletely characterized,
289 particularly in human disease states (24). While recent in situ imaging studies have delineated the spatial
290 organization of murine hematopoiesis under steady-state and stress conditions (25, 26), comparable resolution in
291 the human system has been limited. Building on our prior work establishing a single-cell, whole-slide framework
292 for mapping normal human marrow architecture (7), we applied this approach to MDS to test whether quantitative
293 spatial organization encodes clinically meaningful disease states.
294 Our findings demonstrate that MDS is characterized by coordinated and genotype-imprinted architectural
295 remodeling. Increased proportions of hematopoietic stem and progenitor cells (HSPCs), myeloblasts, and
296 megakaryocytes intensified with disease severity, but these quantitative shifts were accompanied by spatial
297 reorganization not captured by conventional morphology. *TP53*-mutated cases exhibited particularly distinct
298 architectural profiles, including altered erythroid and granulocytic progenitor composition and pronounced
299 megakaryocyte abnormalities. Megakaryocytes are recognized regulators of the marrow niche, influencing
300 thrombopoiesis and HSPC maintenance through paracrine signaling (27, 28), and the marked morphologic
301 perturbations observed in *TP53*-mutated disease suggest genotype-specific niche remodeling.

302 A central architectural alteration in MDS was displacement of HSPCs from perivascular niches. In normal
303 marrow, HSPCs preferentially localize near trabecular bone and CD34-positive endothelial structures, consistent
304 with prior demonstrations of perisinusoidal stem cell enrichment (29). Endothelial cells play a critical role in
305 regulating hematopoietic homeostasis through angiocrine signaling (30–37), and disruption of these interactions
306 has been implicated in hematologic disease (32, 33). In MDS, particularly in *TP53*-mutated cases, HSPCs and
307 early progenitors were selectively displaced from vascular niches. Re-analysis of publicly available
308 transcriptomic and proteomic datasets (13–16) revealed reproducibly reduced CXCR4 expression in MDS HSPCs
309 relative to healthy controls. Given established CXCL12–CXCR4–mediated niche retention mechanisms and
310 reported modulation of CXCR4 by p53 (38), these findings provide a plausible molecular correlate linking cell-
311 intrinsic genetic alterations with large-scale spatial reorganization. Although causality cannot be inferred, the
312 convergence of genotype, gene expression, and spatial displacement supports a model in which clonal evolution
313 is accompanied by niche remodeling.

314 Quantitative spatial analysis also enabled systematic reassessment of historically described morphologic
315 abnormalities in MDS. Disruption of erythroid islands and abnormal progenitor clustering have long been
316 recognized features of dysplastic marrow (17, 21), yet comprehensive spatial quantification has been lacking. We
317 demonstrate that erythroid island disaggregation correlates with anemia severity and occurs in genotype-specific
318 patterns, including prominent disruption in *SF3B1*-mutated low-blast cases. SF3B1 plays a critical role in
319 erythropoiesis through regulation of mRNA splicing (39), and mutation-associated mis-splicing contributes to
320 ineffective erythroid differentiation and anemia (40, 41). Similarly, quantitative assessment of atypical
321 localization of immature precursors (ALIP) revealed spatial heterogeneity within clinically similar high-risk MDS
322 cases, reinforcing the concept that marrow topology reflects underlying genetic programs.

323 Integration of cellular composition, morphologic features, and spatial topology into the MDS
324 Microarchitectural Perturbation Score (MDS-MAPS) provided a unified representation of tissue-level disease
325 state. While MDS-MAPS broadly aligned with IPSS-M categories, discordant cases—particularly among lower-
326 risk patients—suggest that spatial architecture captures dimensions of disease biology not incorporated into

327 current prognostic models. Patch-level analyses further revealed substantial intra-tissue heterogeneity, especially
328 in low-blast MDS, indicating that early disease may involve focal architectural remodeling that could be
329 overlooked in aspirate-based or purely morphologic assessments. Notably, in leave-one-patient-out cross-
330 validation comparing treatment-naïve CCUS and MDS-LB samples, MDS-MAPS demonstrated strong
331 discrimination and outperformed mutation burden–based metrics, including maximum and summed variant allele
332 frequency. This finding suggests that quantitative microarchitectural perturbation distinguishes precursor states
333 from morphologically defined low-blast MDS and captures tissue-level disease biology not reflected by clonal
334 burden alone.

335 Longitudinal analyses underscore the dynamic nature of spatial remodeling. MDS-MAPS decreased
336 consistently in remission samples and discriminated active disease from remission using leave-one-patient-out
337 cross-validation, outperforming blast percentage in both ROC and precision–recall analyses. Mixed-effects
338 modeling confirmed that MAPS reductions occurred independently of blast burden, supporting the interpretation
339 that quantitative architecture represents an orthogonal tissue-state metric. In representative patients, normalization
340 of HSPC localization and progenitor clustering accompanied clinical and genetic remission, with re-emergence
341 of spatial perturbations at relapse. These findings provide proof-of-principle that intact marrow architecture tracks
342 therapeutic response.

343 Exploratory analyses of blast progression suggest that specific spatial parameters—particularly progenitor
344 displacement from vascular niches—may provide additive prognostic information beyond conventional clinical
345 variables. Although limited by cohort size, these observations support prospective evaluation of spatial
346 biomarkers in larger, clinically annotated cohorts.

347 This study has limitations. The sample size, particularly for progression and remission analyses, constrains
348 definitive prognostic conclusions, and mechanistic interpretations of niche disruption remain correlative.
349 Validation in independent and prospectively collected cohorts will be essential to establish clinical utility.
350 Nevertheless, interrogation of millions of spatially resolved cells across diagnostic and longitudinal biopsies
351 provides a high-resolution framework for understanding marrow organization in MDS.

In summary, we demonstrate that quantitative spatial architecture of the human bone marrow encodes genotype, disease severity, and therapeutic response in MDS. By integrating multiplex imaging with computational modeling, we define a tissue-level metric that complements blast-based and molecular assessments. These findings support incorporation of spatially resolved analysis into future diagnostic and translational studies and provide a foundation for evaluating microarchitectural biomarkers in hematologic malignancies.

377 **MATERIALS & METHODS**

378 ***Study Cohort and Clinical Definitions***

379 Archival posterior iliac crest bone marrow trephine biopsies were collected from individuals evaluated
380 for cytopenia of unknown etiology at our academic medical center. All cases were classified according to World
381 Health Organization (WHO) 5th edition criteria. The study was approved by the Institutional Review Board and
382 conducted in accordance with the Declaration of Helsinki.

383 The cohort comprised 49 unique patients with myelodysplastic neoplasms (MDS; n=36) or clonal
384 cytopenia(s) of undetermined significance (n=13), contributing 77 trephine biopsy samples. Twenty-nine serial
385 biopsies from 14 MDS patients (range 2–7 per patient) were obtained after the diagnostic biopsy. Twenty-one
386 normal bone marrow (NBM) controls from a previously published cohort were included. A tissue microarray
387 (TMA) incorporating 7 additional *TP53*-mutated MDS cases and 5 NBMs was included in analyses
388 corresponding to Figures 2–3.

389 Clinical definitions were prespecified and adjudicated prior to development of the MDS
390 Microarchitectural Perturbation Score (MDS-MAPS), and therefore without knowledge of MAPS results.
391 Diagnostic (treatment-naïve) samples were those establishing diagnosis prior to therapy. Serial samples were
392 those obtained after diagnosis. Disease-modifying therapies primarily included hypomethylating agents
393 (azacytidine or decitabine) with or without venetoclax (Supplemental Data Tables 1 and 3).

394 Remission versus active disease status for serial biopsies was determined through integration of 2023
395 International Working Group (IWG) response criteria (42), contemporaneous pathology reports, and concurrent
396 cytogenetic and molecular findings. Biopsies were classified as remission if they met IWG criteria for complete
397 remission (CR) or CR with incomplete hematologic recovery (CRi), including marrow blasts <5%, and were
398 interpreted morphologically as remission without persistent dysplasia or excess blasts. Cases were classified as
399 active disease if driver mutations and/or clonal cytogenetic abnormalities consistent with residual MDS
400 persisted, even when blasts were <5%. Molecular remission was defined as absence of detectable mutations to a

401 sensitivity of 5% variant allele frequency (VAF) using clinically validated non–minimal residual disease
402 targeted sequencing. Blast progression was defined as any increase in marrow blast percentage relative to
403 baseline. Clinical laboratory data were abstracted from medical records.

404

405 ***Clinical Laboratory Characterization***

406 All diagnostic samples underwent standard clinical evaluation including histomorphologic review,
407 multiparameter flow cytometry (MFC), cytogenetic analysis, and targeted next-generation sequencing (NGS).

408 MFC was performed using a 10-color EuroFlow (43) panel with acquisition of ≥200,000 events per
409 sample and analyzed using BD FACSDiva. Blast populations were defined as CD34+/CD117+ cells. Flow-
410 derived proportions were used for orthogonal validation of multiplex immunofluorescence–derived cell types.

411 Conventional cytogenetic analysis was performed on 20 metaphases per case and reported according to
412 International System for Human Cytogenetic Nomenclature guidelines. FISH was performed when clinically
413 indicated using probes targeting recurrent MDS-associated abnormalities.

414 Targeted NGS was performed using either a 45-gene panel (analytical sensitivity ~2% VAF for SNVs,
415 1% for indels) or the TruSight Oncology 500 assay (~3% VAF sensitivity) on Illumina platforms, with analysis
416 using clinically validated pipelines. Mutation status was derived from diagnostic reports.

417

418 ***Multiplex Immunofluorescence Imaging***

419 Multiplex immunofluorescence (MxIF) staining was performed using the Opal platform (Akoya
420 Biosciences) (7, 44, 45). Whole-slide images were acquired on the Vectra Polaris / PhenoImager system at high
421 magnification and spatial resolution sufficient for single-cell segmentation.

422 The antibody panel consisted of CD34, CD117, CD38, CD71, CD61, CD15, and DAPI. For selected
423 analyses, p53 was substituted for CD38. Regions containing <100 cells per 256 × 256 µm patch or >95% non-
424 hematopoietic elements were excluded. All slides underwent visual quality control.

425

426 ***Image Segmentation and Phenotyping***

427 Whole-cell segmentation was performed using the Mesmer deep learning framework (46). Nuclei were
428 identified via DAPI signal and expanded to whole-cell masks using membrane marker information.

429 Cell phenotypes were assigned using convolutional neural network–based classification. Structural
430 elements (trabeculae, adipose tissue, vasculature) were annotated using morphological criteria and CD34 signal
431 for endothelial structures. Segmentation and phenotyping pipelines were applied uniformly across all samples.

432

433 ***Spatial Analyses***

434 Spatial enrichment relative to vasculature and trabeculae was quantified using permutation testing with
435 1,000 permutations. Proximity thresholds were defined a priori as 15 µm for vascular enrichment and 30 µm for
436 trabecular enrichment. P-values were calculated as the proportion of permutations exceeding observed
437 enrichment.

438 Erythroid clustering was quantified using Rolling Signal–based Ripley's K statistic (47) with 256 × 256
439 µm windows and density-based clustering using HDBSCAN (min_cluster_size = 5; min_samples = 3). Atypical
440 localization of immature precursors (ALIP) clusters were defined as ≥2 myeloblasts and/or promyelocytes
441 within 12 µm of one another and located >150 µm from trabeculae and >40 µm from vasculature.

442

443 ***Construction of the MDS Microarchitectural Perturbation Score (MDS-MAPS)***

Whole-slide images were subdivided into 256 × 256 µm patches. For each patch, 82 quantitative features encompassing cell-type proportions, morphologic characteristics, spatial proximity measures, and microenvironmental localization metrics were computed and normalized using z-score scaling. Features were evaluated for importance in stratifying disease state, derived exclusively from diagnostic samples, and weighted accordingly at the patch level. MDS-MAPS was constructed as an additive weighted model incorporating both main effects and curated interaction terms:

$$MAP = \Sigma\,(Z(i) \times W(i)) + \Sigma\,(Z(j) \times Z(k) \times W(jk))$$

where Z(i) represents the z-score of feature i, W(i) its weight, and interaction terms model biologically relevant feature pairs. Model weights were derived using diagnostic samples only and were locked prior to longitudinal and remission analyses. No regularization was applied. Interaction features and weights were curated based on established MDS pathology criteria.

Patch-level MAPS values were aggregated to compute sample-level mean MAPS and normalized entropy to quantify spatial heterogeneity.

CCUS/MDS-LB Discrimination and Remission Classification Modeling

Discrimination of CCUS versus MDS-LB and, separately, remission versus active disease, was evaluated using logistic regression with leave-one-patient-out cross-validation (LOPO-CV). The predictive variable was MAPS, calculated at the sample-level. For remission analysis with serial samples, patient-wise LOPO-CV ensured all timepoints from a held-out patient were excluded from training.

Models used L2 regularization (C = 1) without class weighting. Performance was assessed using area under the receiver operating characteristic curve (AUC) and average precision (AP). For CCUS/MDS-LB discrimination, comparative models included 1) aspirate differential counts for blast percentage alone,

promyelocyte percentage alone, or proerythroblast percentage alone; and 2) highest single mutation VAF and summed VAFs. For remission classification, comparative models included blast percentage alone, MAPS alone, and MAPS + blast%.

Statistical significance of the incremental contribution of MAPS beyond comparator metrics was evaluated using permutation testing (1,000 permutations), with ΔAUC as the test statistic. The p-value was defined as the proportion of permutations with ΔAUC ≥ observed ΔAUC.

Mixed-Effects Modeling

To evaluate whether MAPS reductions occurred independently of blast burden, a linear mixed-effects model was fit:

$$MAPS \sim Remission\ Status + Blast\% + (1|Patient)$$

using statsmodels in Python. A random intercept for patient was included; random slopes were not modeled due to limited within-patient sample size.

Re-analysis of Public Datasets

Public transcriptomic datasets (GSE136816, GSE111085, EGAS00001007568) and proteomic data from Behbehani et al. were re-analyzed to evaluate CXCR4 expression in MDS hematopoietic stem and progenitor cells relative to controls. RNA sequencing data were normalized using trimmed mean of M values (TMM). Differential expression was assessed using generalized linear model likelihood ratio testing with Benjamini–Hochberg correction (FDR < 0.05).

Statistical Analysis

All analyses were performed in Python (v3.11). Non-parametric comparisons used the Mann–Whitney U test, correlations used Spearman's rank coefficient, and multiple testing correction was applied using Benjamini–Hochberg (FDR < 0.05) where appropriate.

492 **LIST OF SUPPLEMENTARY MATERIALS**

493 **Supplementary Methods**

494 *Clinicopathologic and Laboratory Data*

495 *Multiplex Immunofluorescence Tissue Staining*

496 *Image Processing and Segmentation Pipeline*

497 *Cell Phenotyping and Classification*

498 *p53 Classification (TMA)*

499 *Structural Masks Segmentation*

500 *Morphologic Feature Extraction*

501 *Spatial Statistics Implementation (Permutation Testing, Ripley's K, HDBSCAN)*

502 *MDS-MAPS Detailed Implementation*

503 *Remission Classification Modeling*

504 *Blast Progression Modeling*

505 *Mixed-Effects Modeling*

506 *Public Dataset Re-Analysis*

507 **Supplementary Figures**

508 *Supplementary Fig. S1*. Single-cell segmentation, phenotyping, and quantitative validation of the multiplex
509 immunofluorescence analysis pipeline.

510 *Supplementary Fig. S2*. Cell-type frequencies and morphologic characteristics across disease and genotype-
511 defined groups.

512 *Supplementary Fig. S3*. Spatial proximity of hematopoietic cell types to vasculature and trabecular bone.

513 *Supplementary Fig. S4*. Reduced CXCR4 expression in CD34+ progenitors across publicly available MDS
514 transcriptomic and proteomic datasets.

515 *Supplementary Fig. S5*. Quantitative assessment of erythroid island architecture in normal and MDS bone
516 marrow.

517 *Supplementary Fig. S6*. Robustness analysis of atypical localization of immature precursors (ALIP).

518 *Supplementary Fig. S7*. Structure and quality control of the MDS Microarchitectural Perturbation Score (MDS-
519 MAPS).

520 *Supplementary Fig. S8*. Exploratory modeling of baseline predictors of blast count increase.

521 *Supplementary Fig. S9*. Multimodal longitudinal assessment in patients with transient remission.

522

523 **REFERENCES**

524 1. M. Cazzola, Myelodysplastic Syndromes. *N. Engl. J. Med.* **383**, 1358–1374 (2020).

525 2. R. P. Hasserjian, U. Germing, L. Malcovati, Diagnosis and classification of myelodysplastic syndromes.
526 *Blood* **142**, 2247–2257 (2023).

527 3. L. D. Yuen, R. P. Hasserjian, Morphologic Characteristics of Myelodysplastic Syndromes. *Clin. Lab. Med.*
528 **43**, 577–596 (2023).

529 4. E. Bernard, H. Tuechler, P. L. Greenberg, R. P. Hasserjian, O. J. E. Arango, Y. Nannya, S. M. Devlin, M.
530 Creignou, P. Pinel, L. Monnier, G. Gundem, -Martinez Juan S. Medina, D. Domenico, ädersten M. J, U.
531 Germing, G. Sanz, de L. A. A. van, O. Kosmider, M. Y. Follo, F. Thol, L. Zamora, R. F. Pinheiro, A.
532 Pellagatti, H. K. Elias, D. Haase, C. Ganster, L. Ades, M. Tobiasson, L. Palomo, P. M. G. Della, -Kondo
533 Akifumi Takaori, T. Ishikawa, S. Chiba, S. Kasahara, Y. Miyazaki, A. Viale, K. Huberman, P. Fenaux, M.
534 Belickova, M. R. Savona, V. M. Klimek, F. P. S. Santos, J. Boultwood, I. Kotsianidis, V. Santini, é F. Sol, U.
535 Platzbecker, M. Heuser, P. Valent, K. Ohyashiki, C. Finelli, M. T. Voso, L.-Y. Shih, M. Fontenay, J. H. Jansen,
536 J. Cervera, N. Gattermann, B. L. Ebert, R. Bejar, L. Malcovati, M. Cazzola, S. Ogawa, öm-L. E. Hellstr, E.
537 Papaemmanuil, Molecular International Prognostic Scoring System for Myelodysplastic Syndromes. *NEJM*
538 *Evid.* **1**, EVIDoa2200008 (2022).

539 5. A. Mina, S. Pavletic, P. D. Aplan, The evolution of preclinical models for myelodysplastic neoplasms.
540 *Leukemia* **38**, 683–691 (2024).

541 6. R. Munteanu, D. Gulei, C. S. Moldovan, E. Azzoni, L. Belver, R. Feder, S. Pirv, A. D. Buzoianu, H. Einsele,
542 M. Mittelman, G. Ghiaur, R. Hasserjian, C. Tomuleasa, Humanized mouse models in MDS. *Cell Death Dis.* **16**,
543 531 (2025).

544 7. A. Sarachakov, A. Varlamova, V. Svelolkin, M. Polyakova, I. Valencia, C. Unkenholz, T. Pannellini, I.
545 Galkin, P. Ovcharov, D. Tabakov, E. Postovalova, N. Shin, I. Sethi, A. Bagaev, T. Itkin, G. M. Crane, M. J.
546 Kluk, J. T. Geyer, G. G. Inghirami, S. S. Patel, Spatial Mapping of Human Hematopoiesis at Single Cell
547 Resolution Reveals Aging-Associated Topographic Remodeling. *Blood* , blood.2023021280 (2023).

548 8. B. Will, L. Zhou, T. O. Vogler, S. Ben-Neriah, C. Schinke, R. Tamari, Y. Yu, T. D. Bhagat, S.
549 Bhattacharyya, L. Barreyro, C. Heuck, Y. Mo, S. Parekh, C. McMahon, A. Pellagatti, J. Boultwood, C.
550 Montagna, L. Silverman, J. Maciejewski, J. M. Greally, B. H. Ye, A. F. List, C. Steidl, U. Steidl, A. Verma,
551 Stem and progenitor cells in myelodysplastic syndromes show aberrant stage-specific expansion and harbor
552 genetic and epigenetic alterations. *Blood* **120**, 2076–2086 (2012).

553 9. S. Fernandez-Pol, L. Ma, R. S. Ohgami, D. A. Arber, Immunohistochemistry for p53 is a useful tool to
554 identify cases of acute myeloid leukemia with myelodysplasia-related changes that are TP53 mutated, have
555 complex karyotype, and have poor prognosis. *Mod. Pathol. Off. J. U. S. Can. Acad. Pathol. Inc* **30**, 382–392
556 (2017).

557 10. M. Tashakori, T. Kadia, S. Loghavi, N. Daver, R. Kanagal-Shamanna, S. Pierce, D. Sui, P. Wei, F.
558 Khodakarami, Z. Tang, M. Routbort, C. A. Bivins, E. J. Jabbour, L. J. Medeiros, K. Bhalla, H. M. Kantarjian, F.
559 Ravandi, J. D. Khoury, TP53 copy number and protein expression inform mutation status across risk categories
560 in acute myeloid leukemia. *Blood* **140**, 58–72 (2022).

561 11. K. L. McGraw, J. Nguyen, R. S. Komrokji, D. Sallman, N. H. Al Ali, E. Padron, J. E. Lancet, L. C.
562 Moscinski, A. F. List, L. Zhang, Immunohistochemical pattern of p53 is a measure of TP53 mutation burden
563 and adverse clinical outcome in myelodysplastic syndromes and secondary acute myeloid leukemia.
564 *Haematologica* **101**, e320-323 (2016).

565 12. R. Möhle, F. Bautz, S. Rafii, M. A. S. Moore, W. Brugger, L. Kanz, The Chemokine Receptor CXCR-4 Is
566 Expressed on CD34+Hematopoietic Progenitors and Leukemic Cells and Mediates Transendothelial Migration
567 Induced by Stromal Cell-Derived Factor-1. *Blood* **91**, 4523–4530 (1998).

568 13. J.-C. Jann, N. Schmitt, A. Streuer, Q. Xu, V. Riabov, E. Altrock, N. Weimer, V. Nowak, J. Obländer, I.
569 Palme, M. Göl, M. Demmerle, F. Rapp, F. Siegel, L. Steiner, M. Ghazal, A. Duda, V. Haselmann, A. Darwich,
570 A. Jawhar, M. Jawhar, G. Metzgeroth, W.-K. Hofmann, D. Nowak, Instructive interaction between
571 myelodysplastic hematopoiesis and the bone marrow microenvironment at the single-cell level. *Blood*
572 *Neoplasia* **1**, 100021 (2024).

573 14. H. Im, V. Rao, K. Sridhar, J. Bentley, T. Mishra, R. Chen, J. Hall, A. Graber, Y. Zhang, X. Li, G. I. Mias,
574 M. P. Snyder, P. L. Greenberg, Distinct transcriptomic and exomic abnormalities within myelodysplastic
575 syndrome marrow cells. *Leuk. Lymphoma* **59**, 2952–2962 (2018).

576 15. I. Ganan-Gomez, H. Yang, F. Ma, G. Montalban-Bravo, N. Thongon, V. Marchica, G. Richard-Carpentier,
577 K. Chien, G. Manyam, F. Wang, A. Alfonso, S. Chen, C. Class, R. Kanagal-Shamanna, J. P. Ingram, Y. Ogoti,
578 A. Rose, S. Loghavi, P. Lockyer, B. Cambo, M. Muftuoglu, S. Schneider, V. Adema, M. McLellan, J. Garza,
579 M. Marchesini, N. Giuliani, M. Pellegrini, J. Wang, J. Walker, Z. Li, K. Takahashi, J. D. Leverson, C. Bueso-
580 Ramos, M. Andreeff, K. Clise-Dwyer, G. Garcia-Manero, S. Colla, Stem cell architecture drives
581 myelodysplastic syndrome progression and predicts response to venetoclax-based therapy. *Nat. Med.* **28**, 557–
582 567 (2022).

583 16. G. K. Behbehani, R. Finck, N. Samusik, K. Sridhar, W. J. Fantl, P. L. Greenberg, G. P. Nolan, Profiling
584 myelodysplastic syndromes by mass cytometry demonstrates abnormal progenitor cell phenotype and
585 differentiation. *Cytometry B Clin. Cytom.* **98**, 131–145 (2020).

586 17. G. Buesche, H. Teoman, A. Giagounidis, G. Göhring, B. Schlegelberger, A. Ganser, C. Aul, H.-H. Kreipe,
587 Impaired formation of erythroblastic islands is associated with erythroid failure and poor prognosis in a
588 significant proportion of patients with myelodysplastic syndromes. *Haematologica* **101**, e177–e181 (2016).

589 18. H. Kayano, Histopathology in the diagnosis of high-risk myelodysplastic syndromes. *J. Clin. Exp. Hematop.*
590 *JCEH* **58**, 51–60 (2018).

591 19. P. Valent, G. Büsche, I. Theurl, I. Z. Uras, U. Germing, R. Stauder, K. Sotlar, W. Füreder, P. Bettelheim, M.
592 Pfeilstöcker, R. Oberbauer, W. R. Sperr, K. Geissler, J. Schwaller, R. Moriggl, M. C. Béné, U. Jäger, H.-P.
593 Horny, O. Hermine, Normal and pathological erythropoiesis in adults: from gene regulation to targeted
594 treatment concepts. *Haematologica* **103**, 1593–1603 (2018).

595 20. J. Zhang, C. Niu, L. Ye, H. Huang, X. He, W.-G. Tong, J. Ross, J. Haug, T. Johnson, J. Q. Feng, S. Harris,
596 L. M. Wiedemann, Y. Mishina, L. Li, Identification of the haematopoietic stem cell niche and control of the
597 niche size. *Nature* **425**, 836–841 (2003).

598 21. C. De Wolf-Peeters, R. Stessens, V. Desmet, G. Tricot, R. L. Verwilghen, The histological characterization
599 of ALIP in the myelodysplastic syndromes. *Pathol. Res. Pract.* **181**, 402–407 (1986).

600 22. M. G. Della Porta, L. Malcovati, E. Boveri, E. Travaglino, D. Pietra, C. Pascutto, F. Passamonti, R.
601 Invernizzi, A. Castello, U. Magrini, M. Lazzarino, M. Cazzola, Clinical relevance of bone marrow fibrosis and
602 CD34-positive cell clusters in primary myelodysplastic syndromes. *J. Clin. Oncol. Off. J. Am. Soc. Clin. Oncol.*
603 **27**, 754–762 (2009).

604 23. P. L. Greenberg, H. Tuechler, J. Schanz, G. Sanz, G. Garcia-Manero, F. Solé, J. M. Bennett, D. Bowen, P.
605 Fenaux, F. Dreyfus, H. Kantarjian, A. Kuendgen, A. Levis, L. Malcovati, M. Cazzola, J. Cermak, C. Fonatsch,
606 M. M. Le Beau, M. L. Slovak, O. Krieger, M. Luebbert, J. Maciejewski, S. M. M. Magalhaes, Y. Miyazaki, M.
607 Pfeilstöcker, M. Sekeres, W. R. Sperr, R. Stauder, S. Tauro, P. Valent, T. Vallespi, A. A. van de Loosdrecht, U.
608 Germing, D. Haase, Revised International Prognostic Scoring System for Myelodysplastic Syndromes. *Blood*
609 **120**, 2454–2465 (2012).

610 24. Q. Wu, J. Zhang, D. Lucas, Anatomy of Hematopoiesis and Local Microenvironments in the Bone Marrow.
611 Where to? *Front. Immunol.* **12**, 768439 (2021).

612 25. Q. Wu, J. Zhang, S. Kumar, S. Shen, M. Kincaid, C. B. Johnson, Y. S. Zhang, R. Turcotte, C. Alt, K. Ito, S.
613 Homan, B. E. Sherman, T.-Y. Shao, A. Slaughter, B. Weinhaus, B. Song, M. D. Filippi, H. L. Grimes, C. P.
614 Lin, K. Ito, S. S. Way, J. M. Kofron, D. Lucas, Resilient anatomy and local plasticity of naive and stress
615 haematopoiesis. *Nature* **627**, 839–846 (2024).

616 26. J. Zhang, Q. Wu, C. B. Johnson, G. Pham, J. M. Kinder, A. Olsson, A. Slaughter, M. May, B. Weinhaus, A.
617 D'Alessandro, J. D. Engel, J. X. Jiang, J. M. Kofron, L. F. Huang, V. B. S. Prasath, S. S. Way, N. Salomonis,
618 H. L. Grimes, D. Lucas, In situ mapping identifies distinct vascular niches for myelopoiesis. *Nature* **590**, 457–
619 462 (2021).

620 27. F. Puhm, A. Laroche, E. Boilard, Diversity of Megakaryocytes. *Arterioscler. Thromb. Vasc. Biol.* **43**, 2088–
621 2098 (2023).

622 28. S. Di Giandomenico, P. Kermani, N. Mollé, M. M. Yabut, G. Abu-Zeinah, T. Stephens, N. Messali, R.
623 Schreiner, F. Brenet, S. Rafii, J. M. Scandura, Megakaryocyte TGFβ1 partitions erythropoiesis into immature
624 progenitor/stem cells and maturing precursors. *Blood* **136**, 1044–1054 (2020).

625 29. M. Acar, K. S. Kocherlakota, M. M. Murphy, J. G. Peyer, H. Oguro, C. N. Inra, C. Jaiyeola, Z. Zhao, K.
626 Luby-Phelps, S. J. Morrison, Deep imaging of bone marrow shows non-dividing stem cells are mainly
627 perisinusoidal. *Nature* **526**, 126–130 (2015).

628 30. B. Heissig, K. Hattori, S. Dias, M. Friedrich, B. Ferris, N. R. Hackett, R. G. Crystal, P. Besmer, D. Lyden,
629 M. A. S. Moore, Z. Werb, S. Rafii, Recruitment of stem and progenitor cells from the bone marrow niche
630 requires MMP-9 mediated release of kit-ligand. *Cell* **109**, 625–637 (2002).

631 31. S. Rafii, F. Shapiro, R. Pettengell, B. Ferris, R. L. Nachman, M. A. S. Moore, A. S. Asch, Human Bone
632 Marrow Microvascular Endothelial Cells Support Long-Term Proliferation and Differentiation of Myeloid and
633 Megakaryocytic Progenitors. *Blood* **86**, 3353–3363 (1995).

634 32. J. M. Gomez-Salinero, D. Redmond, S. Rafii, Microenvironmental determinants of endothelial cell
635 heterogeneity. *Nat. Rev. Mol. Cell Biol.* **26**, 476–495 (2025).

636 33. S. Pinho, P. S. Frenette, Haematopoietic stem cell activity and interactions with the niche. *Nat. Rev. Mol.*
637 *Cell Biol.* **20**, 303–320 (2019).

638 34. S. T. Avecilla, K. Hattori, B. Heissig, R. Tejada, F. Liao, K. Shido, D. K. Jin, S. Dias, F. Zhang, T. E.
639 Hartman, N. R. Hackett, R. G. Crystal, L. Witte, D. J. Hicklin, P. Bohlen, D. Eaton, D. Lyden, F. de Sauvage, S.
640 Rafii, Chemokine-mediated interaction of hematopoietic progenitors with the bone marrow vascular niche is
641 required for thrombopoiesis. *Nat. Med.* **10**, 64–71 (2004).

642 35. J. M. Butler, D. J. Nolan, E. L. Vertes, B. Varnum-Finney, H. Kobayashi, A. T. Hooper, M. Seandel, K.
643 Shido, I. A. White, M. Kobayashi, L. Witte, C. May, C. Shawber, Y. Kimura, J. Kitajewski, Z. Rosenwaks, I. D.
644 Bernstein, S. Rafii, Endothelial cells are essential for the self-renewal and repopulation of Notch-dependent
645 hematopoietic stem cells. *Cell Stem Cell* **6**, 251–264 (2010).

646 36. A. T. Hooper, J. M. Butler, D. J. Nolan, A. Kranz, K. Iida, M. Kobayashi, H.-G. Kopp, K. Shido, I. Petit, K.
647 Yanger, D. James, L. Witte, Z. Zhu, Y. Wu, B. Pytowski, Z. Rosenwaks, V. Mittal, T. N. Sato, S. Rafii,
648 Engraftment and reconstitution of hematopoiesis is dependent on VEGFR2-mediated regeneration of sinusoidal
649 endothelial cells. *Cell Stem Cell* **4**, 263–274 (2009).

650 37. H. Kobayashi, J. M. Butler, R. O'Donnell, M. Kobayashi, B.-S. Ding, B. Bonner, V. K. Chiu, D. J. Nolan,
651 K. Shido, L. Benjamin, S. Rafii, Angiocrine factors from Akt-activated endothelial cells balance self-renewal
652 and differentiation of haematopoietic stem cells. *Nat. Cell Biol.* **12**, 1046–1056 (2010).

653 38. Q. Li, M. Wang, L. Zeng, W. Guo, Y. Xu, C. Li, Y. Lai, L. Ye, X. Peng, Deletion of Wild-type p53
654 Facilitates Bone Metastatic Function by Blocking the AIP4 Mediated Ligand-Induced Degradation of CXCR4.
655 *Front. Pharmacol.* **12**, 792293 (2021).

656 39. P. L. Moura, T. Mortera-Blanco, I. J. Hofman, G. Todisco, W. W. Kretzschmar, A.-C. Björklund, M.
657 Creignou, M. Hagemann-Jensen, C. Ziegenhain, D. Cabrerizo Granados, I. Barbosa, G. Walldin, M. Jansson, N.
658 Ashley, A. J. Mead, V. Lundin, M. Dimitriou, T. Yoshizato, P. S. Woll, S. Ogawa, R. Sandberg, S. E. W.
659 Jacobsen, E. Hellström-Lindberg, Erythroid Differentiation Enhances RNA Mis-Splicing in SF3B1-Mutant
660 Myelodysplastic Syndromes with Ring Sideroblasts. *Cancer Res.* **84**, 211–225 (2024).

661 40. A. De La Garza, R. C. Cameron, V. Gupta, E. Fraint, S. Nik, T. V. Bowman, The splicing factor Sf3b1
662 regulates erythroid maturation and proliferation via TGFβ signaling in zebrafish. *Blood Adv.* **3**, 2093–2104
663 (2019).

664 41. Y. K. Lieu, Z. Liu, A. M. Ali, X. Wei, A. Penson, J. Zhang, X. An, R. Rabadan, A. Raza, J. L. Manley, S.
665 Mukherjee, SF3B1 mutant-induced missplicing of MAP3K7 causes anemia in myelodysplastic syndromes.
666 *Proc. Natl. Acad. Sci. U. S. A.* **119**, e2111703119 (2022).

667 42. A. M. Zeidan, U. Platzbecker, J. P. Bewersdorf, M. Stahl, L. Adès, U. Borate, D. Bowen, R. Buckstein, A.
668 Brunner, H. E. Carraway, N. Daver, M. Díez-Campelo, T. de Witte, A. E. DeZern, F. Efficace, G. Garcia-
669 Manero, J. S. Garcia, U. Germing, A. Giagounidis, E. A. Griffiths, R. P. Hasserjian, E. Hellström-Lindberg, M.
670 Iastrebner, R. Komrokji, A. G. Kulasekararaj, L. Malcovati, Y. Miyazaki, O. Odenike, V. Santini, G. Sanz, P.
671 Scheinberg, R. Stauder, A. A. van de Loosdrecht, A. H. Wei, M. A. Sekeres, P. Fenaux, Consensus proposal for
672 revised International Working Group 2023 response criteria for higher-risk myelodysplastic syndromes. *Blood*
673 **141**, 2047–2061 (2023).

674 43. J. J. M. van Dongen, L. Lhermitte, S. Böttcher, J. Almeida, V. H. J. van der Velden, J. Flores-Montero, A.
675 Rawstron, V. Asnafi, Q. Lécrevisse, P. Lucio, E. Mejstrikova, T. Szczepański, T. Kalina, R. de Tute, M.
676 Brüggemann, L. Sedek, M. Cullen, A. W. Langerak, A. Mendonça, E. Macintyre, M. Martin-Ayuso, O. Hrusak,
677 M. B. Vidriales, A. Orfao, EuroFlow antibody panels for standardized n-dimensional flow cytometric
678 immunophenotyping of normal, reactive and malignant leukocytes. *Leukemia* **26**, 1908–1975 (2012).

679 44. S. Berry, N. A. Giraldo, B. F. Green, T. R. Cottrell, J. E. Stein, E. L. Engle, H. Xu, A. Ogurtsova, C.
680 Roberts, D. Wang, P. Nguyen, Q. Zhu, S. Soto-Diaz, J. Loyola, I. B. Sander, P. F. Wong, S. Jessel, J. Doyle, D.
681 Signer, R. Wilton, J. S. Roskes, M. Eminizer, S. Park, J. C. Sunshine, E. M. Jaffee, A. Baras, A. M. De Marzo,
682 S. L. Topalian, H. Kluger, L. Cope, E. J. Lipson, L. Danilova, R. A. Anders, D. L. Rimm, D. M. Pardoll, A. S.
683 Szalay, J. M. Taube, Analysis of multispectral imaging with the AstroPath platform informs efficacy of PD-1
684 blockade. *Science* **372**, eaba2609 (2021).

685 45. S. S. Patel, J. L. Weirather, M. Lipschitz, A. Lako, P.-H. Chen, G. K. Griffin, P. Armand, M. A. Shipp, S. J.
686 Rodig, The microenvironmental niche in classic Hodgkin lymphoma is enriched for CTLA-4-positive T cells
687 that are PD-1-negative. *Blood* **134**, 2059–2069 (2019).

688 46. N. F. Greenwald, G. Miller, E. Moen, A. Kong, A. Kagel, T. Dougherty, C. C. Fullaway, B. J. McIntosh, K.
689 X. Leow, M. S. Schwartz, C. Pavelchek, S. Cui, I. Camplisson, O. Bar-Tal, J. Singh, M. Fong, G. Chaudhry, Z.
690 Abraham, J. Moseley, S. Warshawsky, E. Soon, S. Greenbaum, T. Risom, T. Hollmann, S. C. Bendall, L.
691 Keren, W. Graf, M. Angelo, D. Van Valen, Whole-cell segmentation of tissue images with human-level
692 performance using large-scale data annotation and deep learning. *Nat. Biotechnol.* **40**, 555–565 (2022).

693 47. C. P. Healy, F. R. Adler, T. L. Deans, Rolling Signal-based Ripley's K: A new algorithm to identify spatial
694 patterns in histological specimens, 2020.05.21.109314 (2020).

695

696

DATA AVAILABILITY

All data and code will be deposited online (https://github.com/BoneMarrowMxIFImaging/MDS.Manuscript) following formal manuscript review.

AUTHOR CONTRIBUTIONS

Conceptualization: S.P. *Methodology*: R.N., D.R., S.P. *Formal analysis*: R.N., D.R. *Investigation*: R.N., A.K., J.C., A.R., I.V., C.U., J.J., F.S., J.P., C.M., L.Z., D.S., G.R., P.D., J.K., J.F., M.G., N.L., A.C., M.O., P.S., J.G., G.I., S.R., D.R., S.P., *Visualization*: R.N. *Resources*: N.L., G.I., S.R., S.P. *Writing*: R.N., S.P. *Supervision*: D.R., S.P. *Funding acquisition*: S.R., S.P.

FUNDING

S.R is supported by NIH funding (R35HL150809). The other authors have no relevant funding to disclose.

COMPETING INTERESTS

The authors declare no competing interests relevant to this study.

ACKNOWLEDGEMENTS

This work was supported by the Department of Pathology and Laboratory Medicine, Weill Cornell Medical College (start-up funding to S.S.P.). Tissue staining and imaging was performed in the Multiparametric In Situ Imaging (MISI) Laboratory of the Department of Pathology and Laboratory Medicine, Weill Cornell Medical College.

FIGURES & LEGENDS

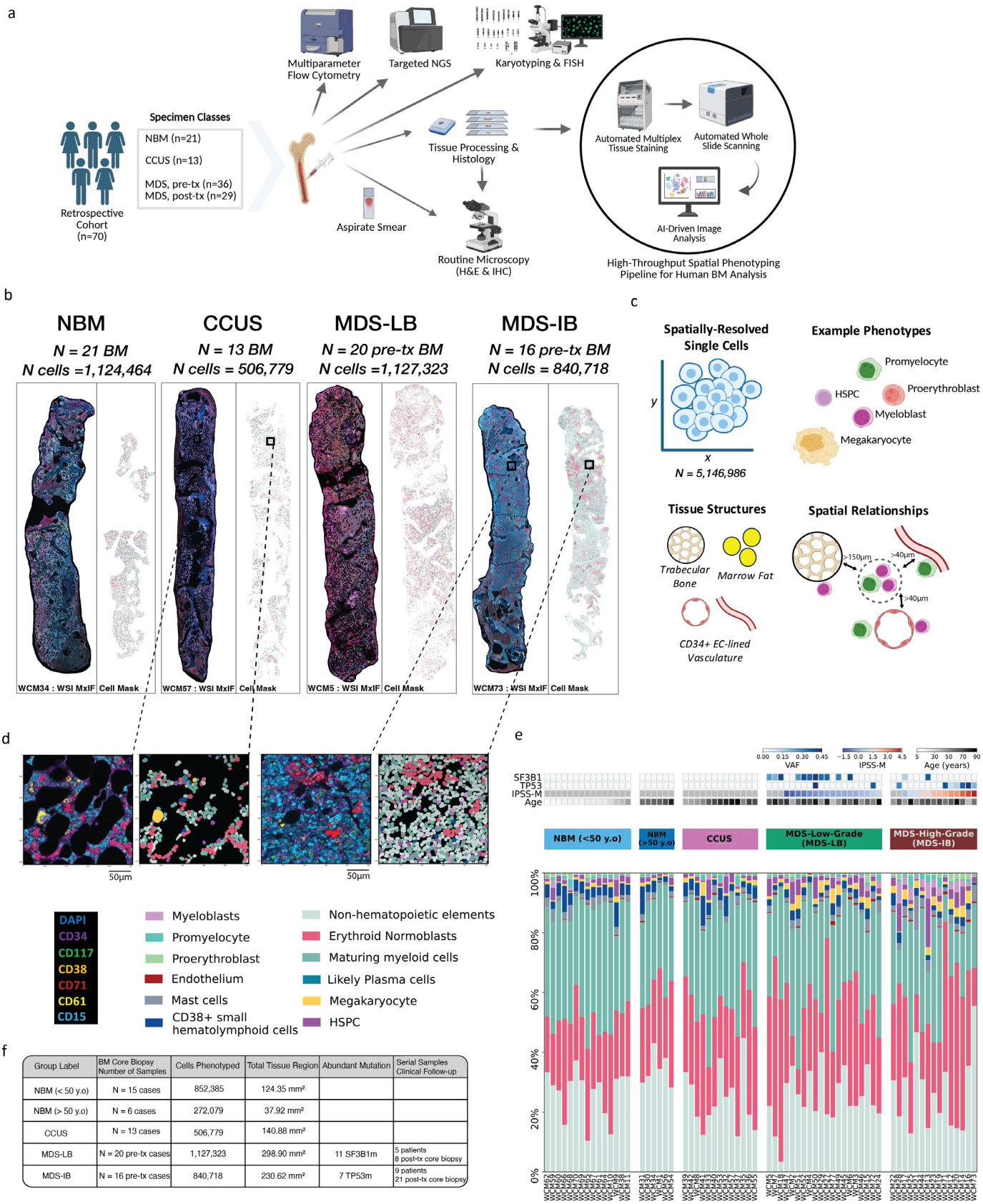

f

Group Label	BM Core Biopsy Number of Samples	Cells Phenotyped	Total Tissue Region	Abundant Mutation	Serial Samples Clinical Follow-up
NBM (< 50 y.o)	N = 15 cases	852,385	124.35 mm²		
NBM (> 50 y.o)	N = 6 cases	272,079	37.92 mm²		
CCUS	N = 13 cases	506,779	140.88 mm²		
MDS-LB	N = 20 pre-tx cases	1,127,323	298.90 mm²	11 SF3B1m	5 patients 8 post-tx core biopsy
MDS-IB	N = 16 pre-tx cases	840,718	230.62 mm²	7 TP53m	9 patients 21 post-tx core biopsy

Figure 1. Study design and single-cell spatial profiling of bone marrow trephine biopsies in MDS.

(a) Schematic of cohort assembly and multiplex immunofluorescence (MxIF) workflow for whole-slide bone marrow trephine biopsy analysis.

(b) Representative whole-slide MxIF images and corresponding single-cell segmentation maps from treatment-naïve samples. MDS cases were categorized as low blast (MDS–low grade; MDS-LB) or high blast (MDS–high grade; MDS-IB). Non-MDS samples included clonal cytopenia of undetermined significance (CCUS) and normal bone marrow (NBM; <50 years or ≥50 years).

(c) Schematic of cellular and spatial features extracted for downstream quantitative analysis.

(d) Representative region of interest (ROI) showing multiplex immunofluorescence channels alongside the corresponding cell-level phenotyped segmentation map from two example cases. Antibody color channel assignments and phenotype definitions are indicated.

(e) Distribution of cell type proportions across the treatment-naïve cohort. Twelve cell phenotypes were defined using membrane marker expression and morphologic parameters.

(f) Cohort characteristics and sample distribution, including number of cases per group, total cells phenotyped, total tissue area analyzed, most frequent mutation per disease group, and number of serial samples included in the longitudinal treatment cohort.

720

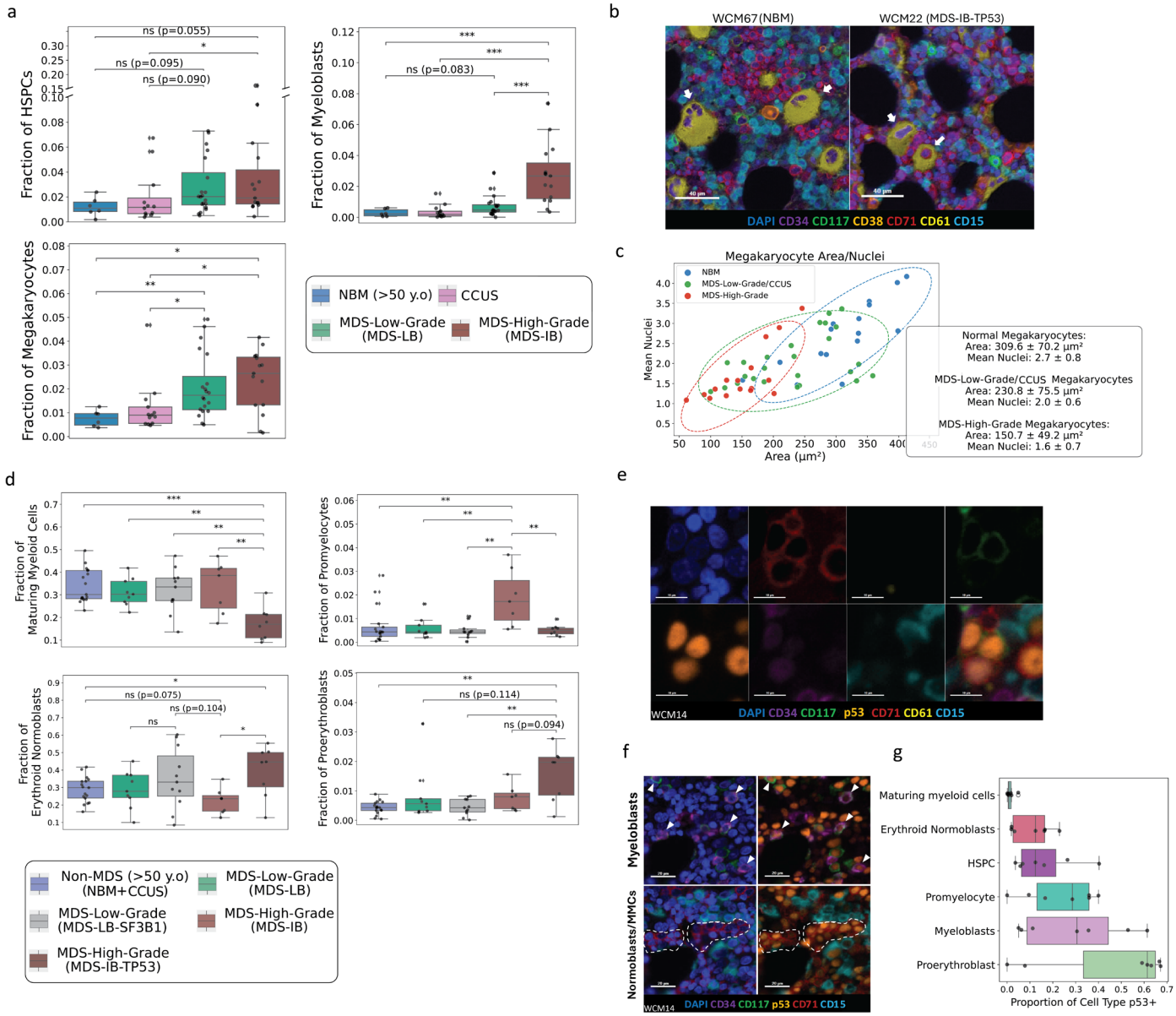

Figure 2. Single-cell compositional and morphologic alterations in MDS.

(a) Proportions of hematopoietic stem and progenitor cells (HSPCs), myeloblasts, and megakaryocytes across primary sample groups. Statistical comparisons were performed using two-sided Mann–Whitney U tests (*P ≤ 0.05, **P ≤ 0.01, ***P ≤ 0.001).

(b) Representative multiplex immunofluorescence (MxIF) images from normal bone marrow (NBM) and MDS samples illustrating differences in megakaryocyte size and morphology (scale bars, 40 µm).

(c) Quantification of mean megakaryocyte area and nuclear number across progression from NBM to CCUS, MDS–low blast (MDS-LB), and MDS–increased blast (MDS-IB). Data are shown as scatter plots with standard deviation ellipses.

(d) Proportions of maturing myeloid cells (MMCs), promyelocytes, proerythroblasts, and erythroid normoblasts across sample groups, with MDS-IB stratified by *TP53* mutation status (two-sided Mann–Whitney U test; *P ≤ 0.05, **P ≤ 0.01, ***P ≤ 0.001).

(e) Representative cluster of $CD117^{+}CD71^{+}$ proerythroblasts with high p53 protein expression from a *TP53*-mutated case (WCM14). Top row (left to right): DAPI (blue), CD71 (red), CD61 (yellow), CD117 (green). Bottom row: p53 (orange), CD34 (magenta), CD15 (cyan), merged image (scale bars, 10 µm).

(f) Representative MxIF image showing myeloblasts and erythroid normoblasts with elevated p53 protein expression in a *TP53*-mutated sample (scale bars, 20 µm).

(g) Proportion of cells with high p53 protein expression across *TP53*-mutated MDS samples in a tissue microarray. Cells were pooled across *TP53*-mutated cases, and proportions were calculated as the number of $p53^{+}$ cells within each phenotype divided by the total number of cells of that phenotype. All MxIF images were acquired using Phenochart (v1.1, Akoya Biosciences).

721

722

723

724

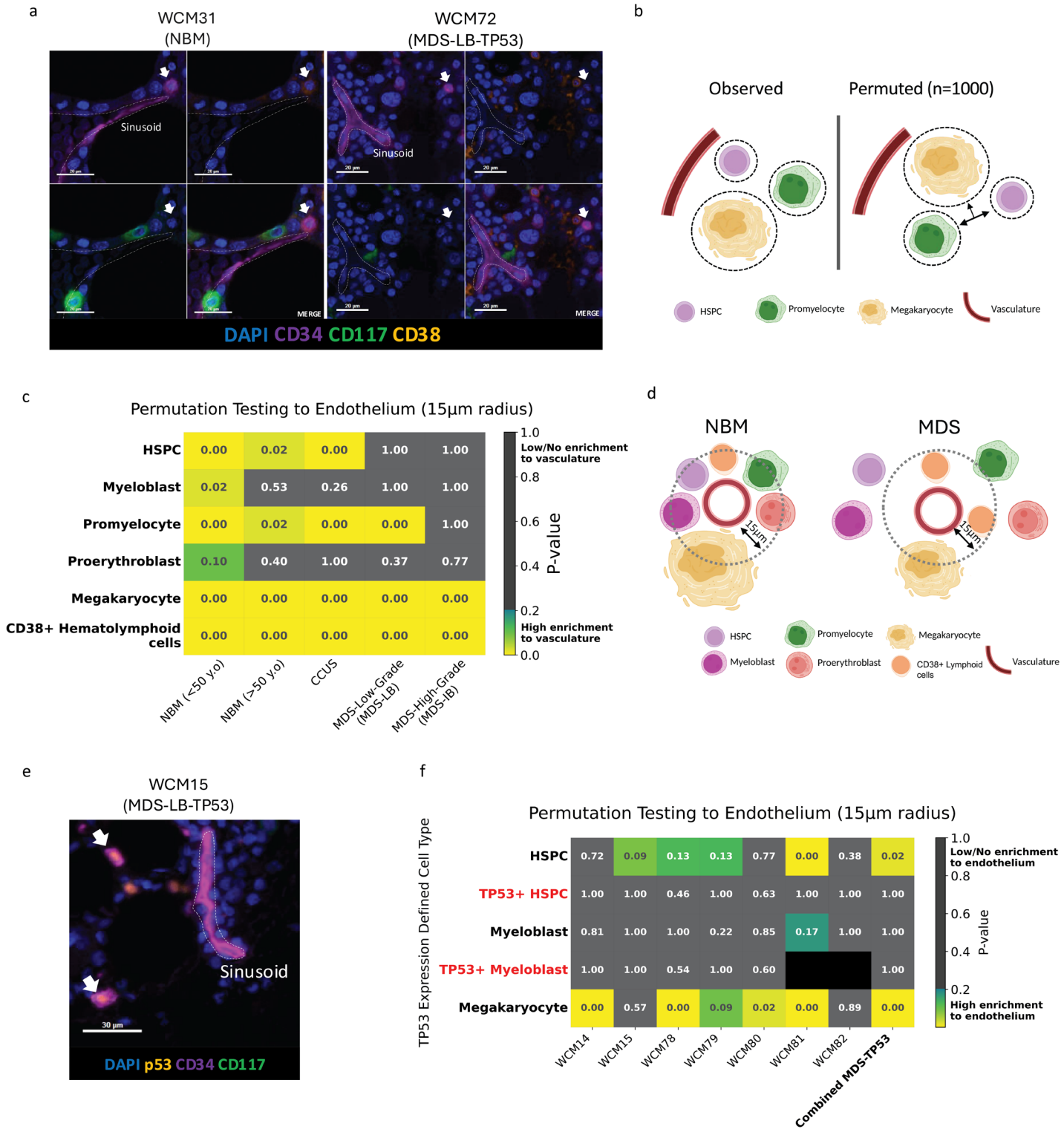

Figure 3. Hematopoietic stem and progenitor cells (HSPCs) show reduced perivascular enrichment along progression from clonal hematopoiesis to overt MDS.

(a) Representative multiplex immunofluorescence (MxIF) images demonstrating localization of HSPCs (arrows) adjacent to $CD34^+$ endothelium in normal bone marrow (NBM) and reduced perivascular association in MDS (scale bars, 20 µm).

(b) Schematic of the permutation-based spatial analysis framework used to assess cell-type enrichment within defined vascular neighborhoods (created with BioRender).

(c) Heatmap of combined P values representing enrichment of indicated cell types within a 15-µm radius of endothelium. For each whole-slide image, 1,000 phenotype-label permutations were performed to generate a null distribution of random spatial assignments. P values were calculated at the patient level and combined across cases within each group using Stouffer's method. Lower values (yellow) indicate significant perivascular enrichment relative to the permuted null distribution, whereas higher values (gray) indicate absence of enrichment or relative displacement from endothelium.

(d) Conceptual schematic summarizing alterations in perivascular niche composition observed in NBM versus MDS (created with BioRender).

(e) Representative MxIF image from a *TP53*-mutated MDS sample showing HSPCs with high p53 protein expression (arrows) exhibiting reduced proximity to endothelium (scale bars, 30 µm).

(f) Permutation testing heatmap from the tissue microarray cohort evaluating vascular enrichment of cell subsets stratified by p53 expression. As in (C), enrichment was assessed using 1,000 phenotype-label permutations per whole-slide image, with patient-level P values combined using Stouffer's method. Lower values (yellow) indicate significant enrichment within 15 µm of endothelium, and higher values (gray) indicate relative displacement.

725

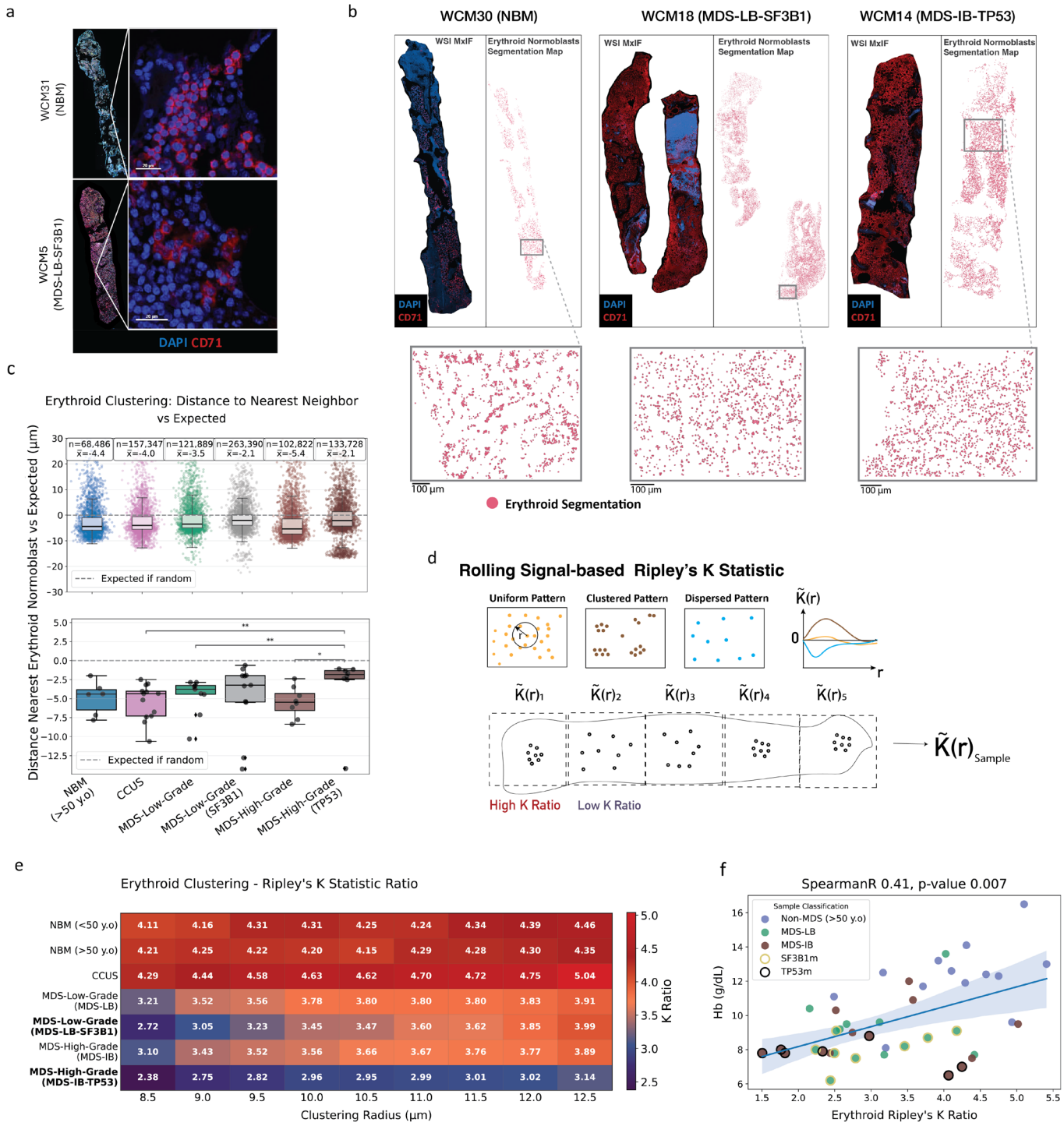

Figure 4. Disrupted erythroid island organization and reduced spatial clustering in MDS.

(a) Representative MxIF images demonstrating a well-formed, densely aggregated erythroid island in normal bone marrow (NBM; top) and dispersed erythroid normoblasts in an MDS-LB–*SF3B1*–mutated sample (bottom) (scale bars, 20 µm).

(b) Whole-slide images showing merged DAPI and CD71 channels (left) and corresponding erythroid normoblast segmentation masks (right) for representative cases from NBM, MDS-LB–*SF3B1*, and MDS-IB–*TP53* groups. Insets display higher-magnification regions of interest (ROIs) highlighting differences in erythroid spatial organization.

(c) Quantification of erythroid normoblast spatial proximity. *Top*: single-cell–level distribution of nearest-neighbor distance between erythroid normoblasts normalized to expected distance relative to all other cell types. *Bottom*: patient-level aggregated distributions. Statistical comparisons were performed using the Mann–Whitney U test (*$P \leq 0.05$, **$P \leq 0.01$).

(d) Schematic illustrating implementation of Rolling Signal–based Ripley's K statistic (RSRK) across whole-slide images using sliding windows (256 × 256 µm, 50% overlap) to quantify multiscale erythroid clustering.

(e) Heatmap showing mean RSRK values across genotype-defined groups evaluated over radii ranging from 8.5 to 12.5 µm. Lower K values indicate reduced spatial clustering (greater dispersion). MDS-LB–*SF3B1* and MDS-IB–*TP53* samples demonstrate consistently reduced clustering across radii.

(f) Scatter plot showing the relationship between erythroid clustering (mean RSRK) and hemoglobin concentration across MDS and age-matched non-MDS cases. A positive correlation was observed (Spearman $r = 0.41$, $P = 0.007$). MDS-LB–*SF3B1* (yellow) and MDS-IB–*TP53* (black) samples are characterized by lower hemoglobin values and reduced erythroid spatial clustering.

726

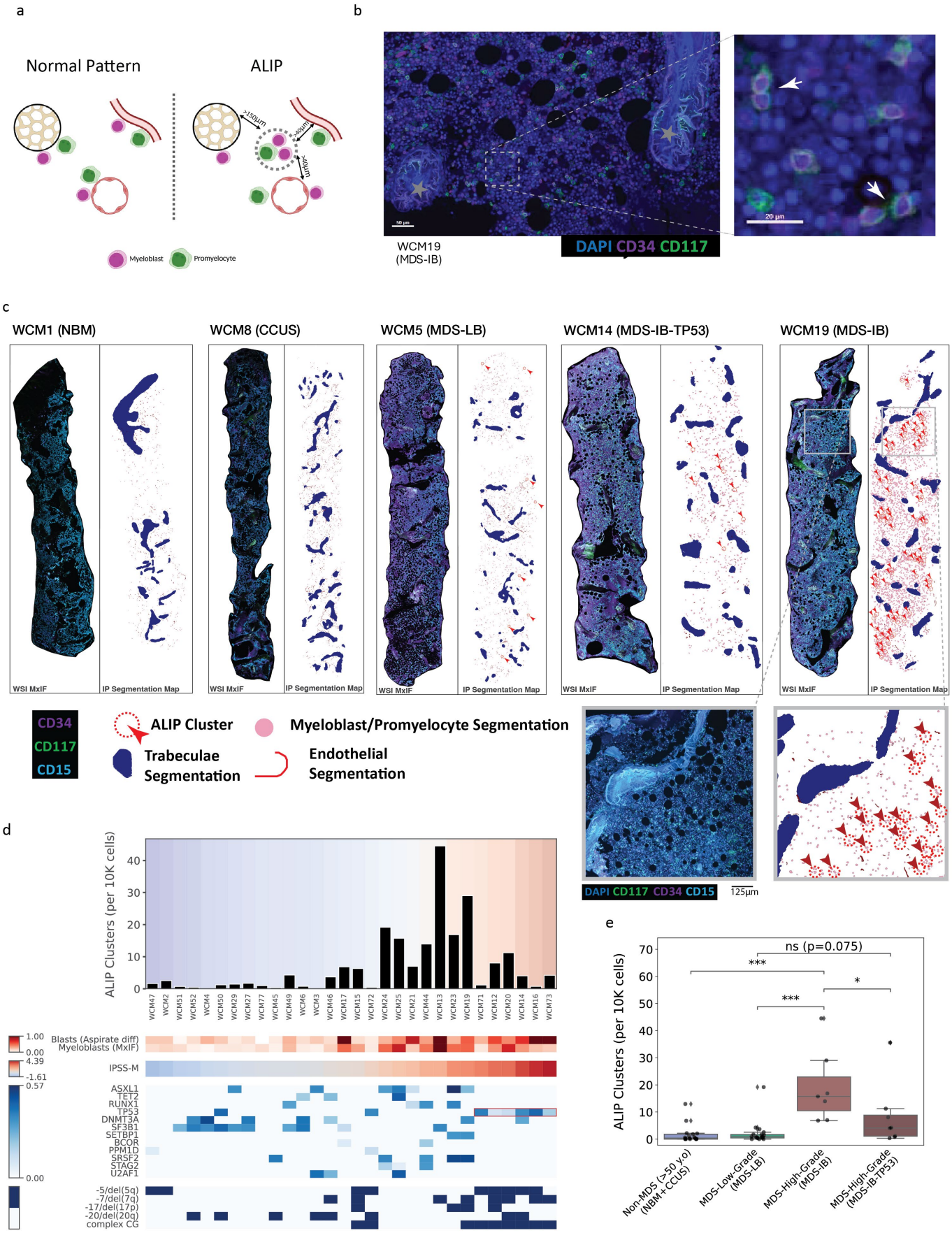
a
Normal Pattern
ALIP
>150µm
>40µm
>40µm
Myeloblast
Promyelocyte
b
WCM19
(MDS-IB)
DAPI CD34 CD117
50 µm
20 µm
c
WCM1 (NBM)
WCM8 (CCUS)
WCM5 (MDS-LB)
WCM14 (MDS-IB-TP53)
WCM19 (MDS-IB)
WSI MxIF
IP Segmentation Map
CD34
CD117
CD15
ALIP Cluster
Trabeculae Segmentation
Myeloblast/Promyelocyte Segmentation
Endothelial Segmentation
DAPI CD117 CD34 CD15
125µm
d
ALIP Clusters (per 10K cells)
Blasts (Aspirate diff)
Myeloblasts (MxIF)
IPSS-M
ASXL1
TET2
RUNX1
TP53
DNMT3A
SF3B1
SETBP1
BCOR
PPM1D
SRSF2
STAG2
U2AF1
-5/del(5q)
-7/del(7q)
-17/del(17p)
-20/del(20q)
complex CG
e
ALIP Clusters (per 10K cells)
ns (p=0.075)
***
***
*
Non-MDS (>50 y.o) (NBM+CCUS)
MDS-Low-Grade (MDS-LB)
MDS-High-Grade (MDS-IB)
MDS-High-Grade (MDS-IB-TP53)

Figure 5. Atypical localization of immature precursors (ALIP) associates with disease severity and distinguishes TP53-mutated high-risk MDS.

(a) Schematic illustrating computational identification of ALIP clusters, defined as groups of ≥2 myeloblasts and/or promyelocytes located >150 µm from trabecular bone and >40 µm from vasculature (designed with BioRender).

(b) Representative MxIF image from an MDS-IB case showing clusters of immature precursors in intertrabecular regions distant from bone and endothelium (scale bar, 50 µm). Arrows denote ALIP clusters in the magnified inset (scale bar, 20 µm). Star symbols indicate bone trabeculae.

(c) Whole-slide examples showing merged CD117, CD34, and CD15 channels (left) and corresponding segmentation maps (right) with bone trabeculae (dark blue), endothelium (dark red), and myeloblast and/or promyelocyte segmentations (gray/pink). ALIP clusters are annotated with red arrows. Representative cases are shown from NBM, CCUS, MDS-LB, MDS-IB–*TP53*, and MDS-IB (*TP53*–wild-type) groups.

(d) Sample-level quantification of ALIP cluster frequency in MDS cases, normalized as number of ALIP clusters per 10,000 total nucleated cells per whole-slide image. Heatmaps beneath each bar display corresponding aspirate smear blast percentage (manual count), MxIF-derived myeloblast proportion, IPSS-M risk category, selected driver mutation variant allele frequency, and cytogenetic abnormalities.

(e) ALIP frequency increases with disease grade and is highest in *TP53*-WT samples among MDS-IB patients (Mann–Whitney U test; *P ≤ 0.05, **P ≤ 0.01, ***P ≤ 0.001).

727

728

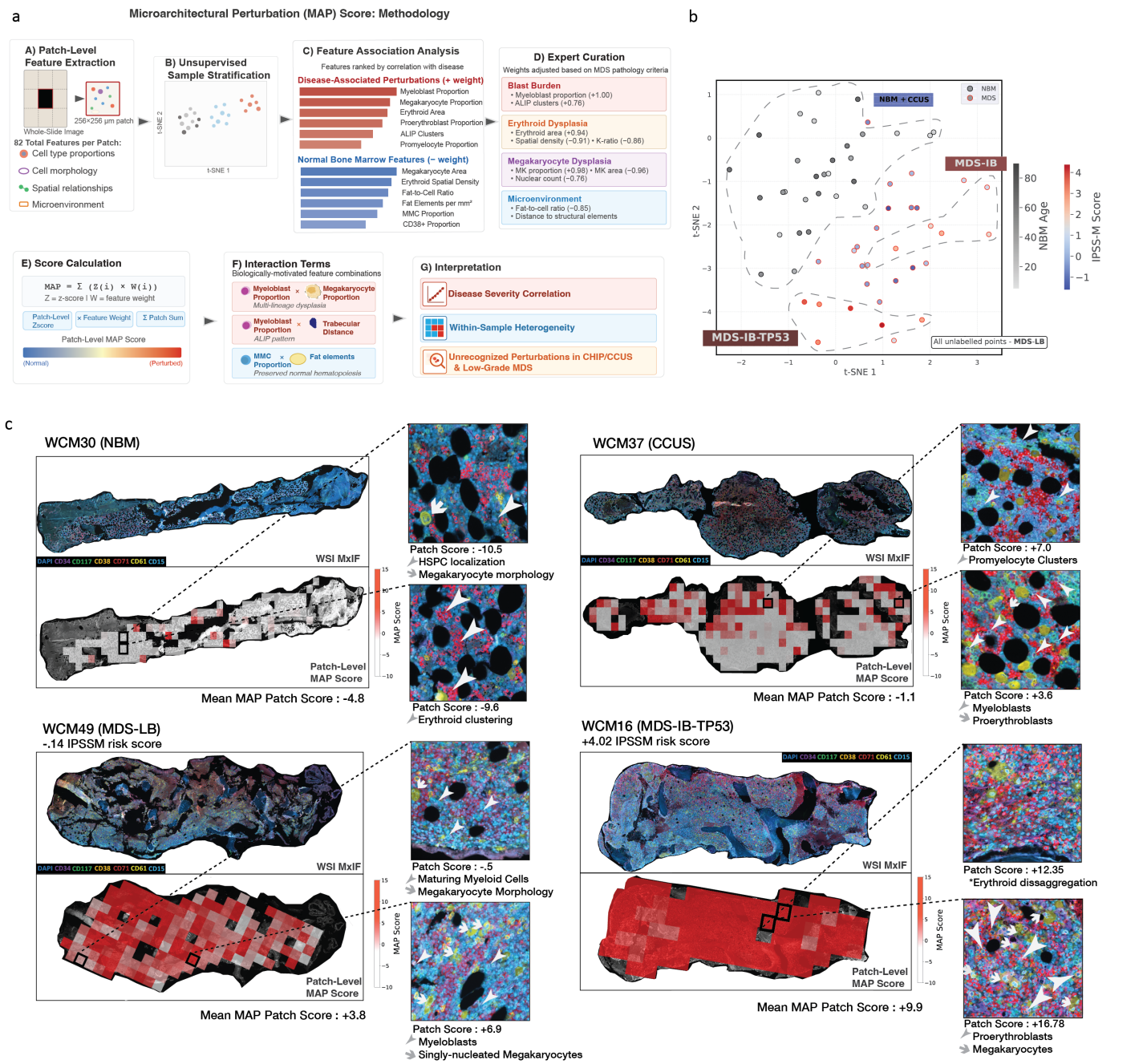
a
Microarchitectural Perturbation (MAP) Score: Methodology
A) Patch-Level Feature Extraction
256×256 µm patch
Whole-Slide Image
82 Total Features per Patch:
Cell type proportions
Cell morphology
Spatial relationships
Microenvironment
B) Unsupervised Sample Stratification
t-SNE 1
t-SNE 2
C) Feature Association Analysis
Features ranked by correlation with disease
Disease-Associated Perturbations (+ weight)
Myeloblast Proportion
Megakaryocyte Proportion
Erythroid Area
Proerythroblast Proportion
ALIP Clusters
Promyelocyte Proportion
Normal Bone Marrow Features (− weight)
Megakaryocyte Area
Erythroid Spatial Density
Fat-to-Cell Ratio
Fat Elements per mm²
MMC Proportion
CD38+ Proportion
D) Expert Curation
Weights adjusted based on MDS pathology criteria
Blast Burden
• Myeloblast proportion (+1.00)
• ALIP clusters (+0.76)
Erythroid Dysplasia
• Erythroid area (+0.94)
• Spatial density (−0.91) • K-ratio (−0.86)
Megakaryocyte Dysplasia
• MK proportion (+0.98) • MK area (−0.96)
• Nuclear count (−0.76)
Microenvironment
• Fat-to-cell ratio (−0.85)
• Distance to structural elements
E) Score Calculation
MAP = Σ (Z(i) × W(i))
Z = z-score | W = feature weight
Patch-Level Zscore
× Feature Weight
Σ Patch Sum
Patch-Level MAP Score
(Normal)
(Perturbed)
F) Interaction Terms
Biologically-motivated feature combinations
Myeloblast Proportion × Megakaryocyte Proportion
Multi-lineage dysplasia
Myeloblast Proportion × Trabecular Distance
ALIP pattern
MMC Proportion × Fat elements
Preserved normal hematopoiesis
G) Interpretation
Disease Severity Correlation
Within-Sample Heterogeneity
Unrecognized Perturbations in CHIP/CCUS & Low-Grade MDS
b
NBM
MDS
NBM + CCUS
MDS-IB
MDS-IB-TP53
All unlabelled points - MDS-LB
t-SNE 1
t-SNE 2
NBM Age
IPSS-M Score
c
WCM30 (NBM)
WSI MxIF
Patch-Level MAP Score
Mean MAP Patch Score : -4.8
Patch Score : -10.5
HSPC localization
Megakaryocyte morphology
Patch Score : -9.6
Erythroid clustering
WCM37 (CCUS)
Mean MAP Patch Score : -1.1
Patch Score : +7.0
Promyelocyte Clusters
Patch Score : +3.6
Myeloblasts
Proerythroblasts
WCM49 (MDS-LB)
-.14 IPSSM risk score
Mean MAP Patch Score : +3.8
Patch Score : -.5
Maturing Myeloid Cells
Megakaryocyte Morphology
Patch Score : +6.9
Myeloblasts
Singly-nucleated Megakaryocytes
WCM16 (MDS-IB-TP53)
+4.02 IPSSM risk score
Mean MAP Patch Score : +9.9
Patch Score : +12.35
*Erythroid dissaggregation
Patch Score : +16.78
Proerythroblasts
Megakaryocytes
MAP Score
d
Patch-Level MAP Score
Mean Patch-Level MAP Score
NBM (>50 y.o)
CCUS
IPSS-M Score
e
Mean MAP Score
Sample-Level Entropy
Non-MDS (>50 y.o) (NBM + CCUS)
MDS-Low-Grade (MDS-LB)
MDS-High-Grade (MDS-IB)
MDS-High-Grade (MDS-IB-TP53)
ns
***
**

Figure 6. Derivation and visualization of the MDS Microarchitectural Perturbation Score (MDS-MAPS).

(a) Schematic illustrating the derivation of MDS-MAPS. Whole-slide images were subdivided into 256 × 256 µm patches, from which 82 predefined cellular and spatial features were extracted. Feature values were standardized and combined in a weighted additive model to generate patch-level perturbation scores. Weights were derived using diagnostic samples and fixed prior to longitudinal analyses.

(b) t-Distributed stochastic neighbor embedding (t-SNE) of sample-level feature vectors showing separation of MDS-LB, MDS-IB and MDS-IB–*TP53* cases from NBM and CCUS samples. NBM samples are color-scaled by age; MDS samples are color-scaled by IPSS-M risk scores.

(c) Representative whole-slide MxIF images (top) and corresponding patch-level MDS-MAPS heatmaps (bottom) for NBM, CCUS, MDS-LB, and MDS-IB–*TP53* cases. White patches indicate low perturbation (low MAPS); red patches indicate high perturbation (high MAPS). Insets show representative 256 × 256 µm patches (dotted outlines) with example features contributing to elevated patch-level scores.

(d) Mean MDS-MAPS per sample across the cohort. NBM and CCUS samples are shown in gray; MDS samples are color-coded by IPSS-M risk scores.

(e) Comparison of sample-level mean MDS-MAPS (left) and normalized entropy of patch-level MAPS distributions (right), reflecting spatial heterogeneity of architectural perturbation (Mann–Whitney U test; *$P \leq 0.05$, **$P \leq 0.01$, ***$P \leq 0.001$).

729

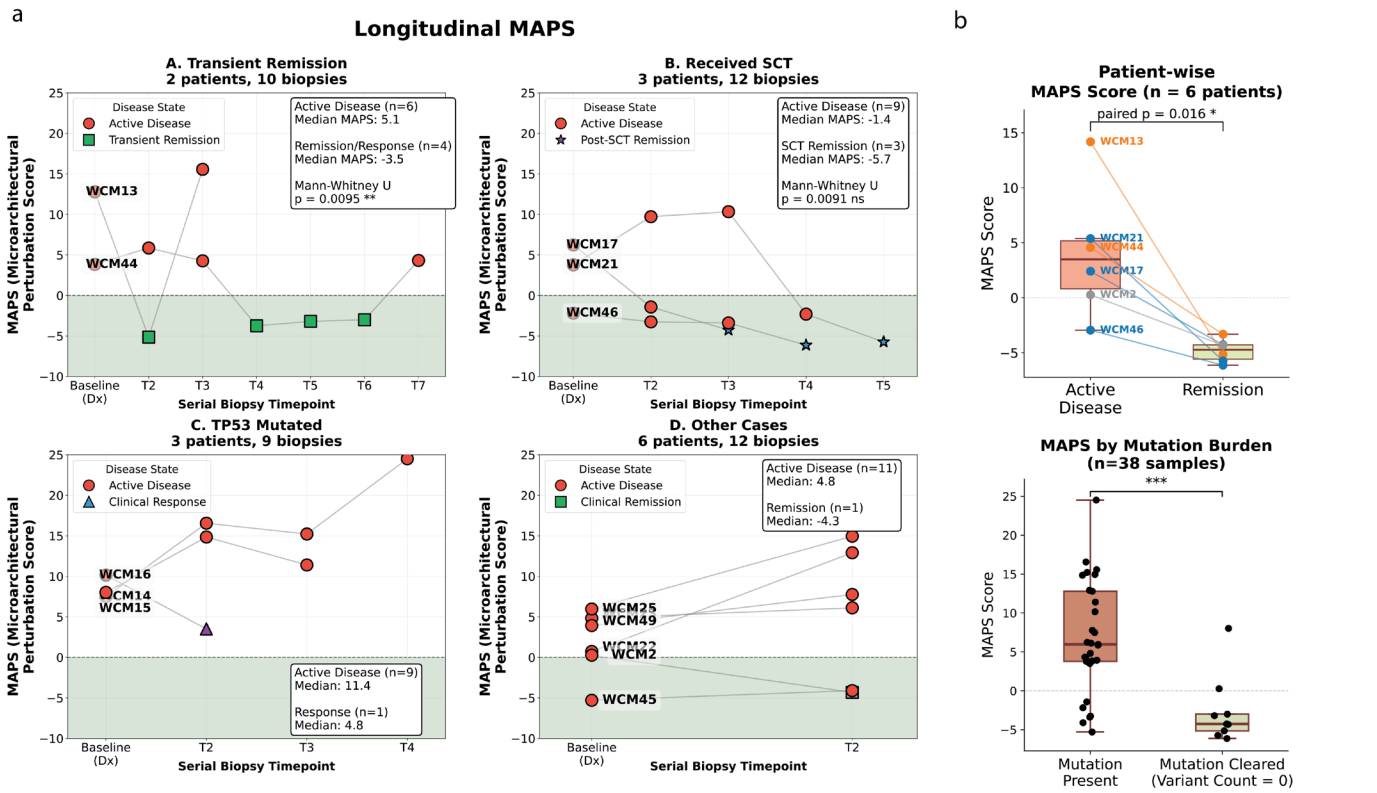

c

Classifying Remission Status (Patient-wise LOOCV)

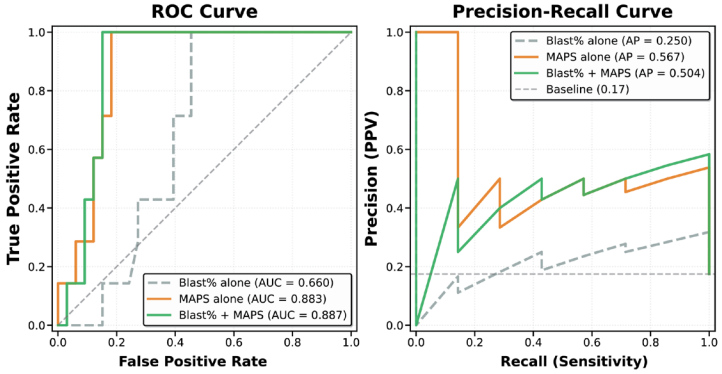

d

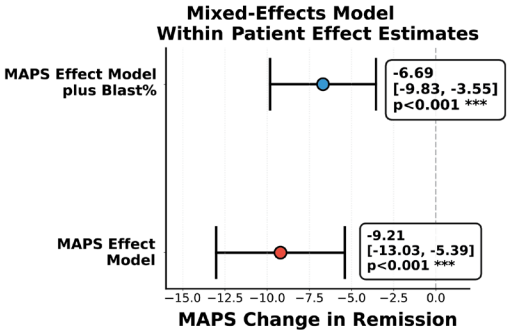

All remission samples (SCT and Non-SCT) included for LOPO-CV

Stratified Analysis by Remission Type:

Non-SCT Remission	**Post-SCT Remission**
(n=38 samples: 5 remission, 33 active)	(n=35 samples: 3 remission, 32 active)
Blast% alone: AUC = 0.655	Blast% alone: AUC = 0.724
MAPS alone: AUC = 0.861	MAPS alone: AUC = 0.917
Combined: AUC = 0.873	Combined: AUC = 0.917
ΔAUC = +0.218	ΔAUC = +0 193

Patient Group
- Transient Remission
- TP53 Mutated
- Received SCT
- Other Cases

e

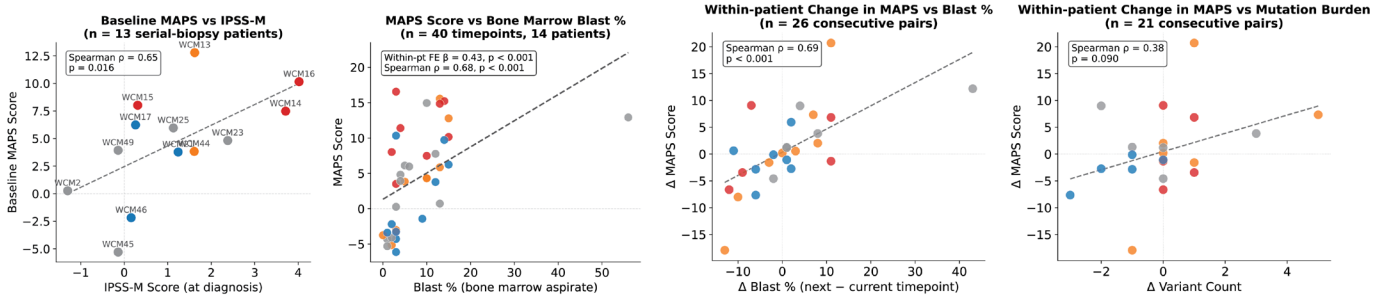

Figure 7. MDS-MAPS discriminates remission and tracks longitudinal disease dynamics in serial MDS biopsies.

(A) Longitudinal MAPS trajectories in patients with serial biopsies. Lines connect sequential samples; dashed line indicates MAPS = 0. Transient remission cases (WCM13, WCM44; n = 2 patients, 10 biopsies) showed marked MAPS reduction at remission (active median = 5.1, n = 6; remission median = −3.5, n = 4; P = 0.0095). Post–stem cell transplantation (SCT) remission cases (WCM17, WCM21, WCM46; n = 3 patients, 12 biopsies) demonstrated similar reductions (active median = −1.4, n = 9; remission median = −5.7, n = 3; P = 0.0091). *TP53*-mutated cases (WCM14–16; n = 3 patients, 9 biopsies) showed persistently elevated MAPS (median = 11.4).

(B) *Top*: Paired within-patient comparison (n = 6) demonstrating reduced MAPS in remission (active median = 5.5; remission median = −4.6; Wilcoxon P = 0.016). *Bottom*: MAPS stratified by molecular remission (n = 38); mutation-cleared samples showed lower MAPS (median = −3.2) than mutation-persistent samples (median = 7.5; ***P < 0.001).

(C) Leave-one-patient-out cross-validation (LOPO-CV) for remission classification (n = 40 samples, 14 patients, 7 remission events). ROC: blast% AUC = 0.660; MAPS AUC = 0.883; combined AUC = 0.887. Precision–recall: MAPS AP = 0.567; blast% + MAPS AP = 0.304; blast% AP = 0.250. MAPS improved discrimination in both non-SCT (ΔAUC = +0.218) and post-SCT (ΔAUC = +0.193) subsets.

(D) Linear mixed-effects models (n = 43 biopsies, 14 patients) demonstrated independent association of MAPS with remission after adjusting for blast% (β = −6.69 [95% CI −9.83, −3.55], P < 0.001); MAPS alone β = −9.21 [−11.03, −5.39], P < 0.001.

(E) MAPS correlated with IPSS-M at baseline (n = 13; ρ = 0.65, P = 0.016) and with blast% across serial samples (within-patient ρ = 0.43; between-patient ρ = 0.68; both P < 0.001). Within-patient ΔMAPS correlated with Δblast% (n = 26 pairs; ρ = 0.69, P < 0.001) but not significantly with Δmutation count (n = 21 pairs; ρ = 0.38, P = 0.090).

730